Coupling into Hyperbolic Carbon-Nanotube Films with a Deep-Etched Antenna Grating

Bryant B. Jerome,[1,2,†] Ciril S. Prasad,[1,2,†] Andrea Schirato,[1,3,4,†] Oliver S. Dewey,[5,6,7,8,9] Jacques Doumani,[1,2] Andrey Baydin,[1,8] Weilu Gao,[10,9] Giuseppe Della Valle,[3,11] Junichiro Kono,[1,7,8,12] Matteo Pasquali,[5,6,7,8,9] Gururaj V. Naik,[*,1] and Alessandro Alabastri[*,1]

[1] *Department of Electrical and Computer Engineering, Rice University, Houston, Texas 77005, USA*

[2] *Applied Physics Graduate Program, Smalley-Curl Institute, Rice University, Houston, Texas, 77005, USA*

[3] *Department of Physics, Politecnico di Milano, Piazza Leonardo da Vinci, 32, 20133 Milano, Italy*

[4] *Istituto Italiano di Tecnologia, via Morego 30, 16163, Genoa, Italy*

[5] *Department of Chemical and Biomolecular Engineering, Rice University, Houston, Texas 77005, USA*

[6] *Department of Chemistry, Rice University, Houston, Texas, 77005, USA*

[7] *Department of Material Science and NanoEngineering, Rice University, Houston, Texas 77005, USA*

[8] *Smalley-Curl Institute, Rice University, Houston, Texas, 77005, USA*

[9] *The Carbon Hub, Rice University, Houston, Texas, 77005, USA*

[10] *Department of Electrical and Computer Engineering, The University of Utah, Salt Lake City, UT, USA*

[11] *Istituto di Fotonica e Nanotecnologie - Consiglio Nazionale delle Ricerche, Piazza Leonardo da Vinci, 32, I-20133 Milano, Italy*

[12] *Department of Physics and Astronomy, Rice University, Houston, Texas 77005, USA*

[†] *Contributed equally to this work*

* E-mail: guru@rice.edu; alabastri@rice.edu

Abstract

Macroscopic films of aligned and packed carbon nanotubes are known to act as broadband hyperbolic materials in the infrared, but methods for efficiently coupling light with high-k modes supported by such materials are currently absent. Here we describe a deep diffraction grating structure fabricated by directly etching a thick wafer-scale film of densely aligned carbon nanotubes. This novel architecture displayed hyperbolic dispersion relations in an ultrabroadband infrared spectral range, with an epsilon near zero point tunable via doping and annealing. Using systematic finite element analysis, we obtained the key geometrical and optical parameters that determine the absorption and emission efficiency of the structure, clarifying the important role of cavity mode generation in the deep-etched grating via confined hyperbolic plasmon polariton excitation. While addressing the question of how to satisfy coupling requirements and further enhance the light–matter interaction strength, we found that properly designed deep grating grooves should allow optical coupling with arbitrarily thick hyperbolic metamaterials, suggesting a strategy for large-scale applications.

Introduction

Hyperbolic materials (HMs) have been attracting interest in the nanophotonics community owing to their peculiar anisotropic optical behavior. Over selected frequency bands, HMs feature an optical permittivity that depends on the incident light polarization, with dielectric-like and metal-like responses along different directions.[1–3] This anisotropic optical dispersion allows HMs to support propagating electromagnetic (EM) modes with indefinite wavevector magnitudes.[1] For example, consider a uniaxial hyperbolic medium such that $\varepsilon'_{xx} < 0$ and $\varepsilon'_{yy} = \varepsilon'_{zz} > 0$, where ε'_{xx}, ε'_{yy}, and ε'_{zz} are the real electric permittivities along the x, y, and z directions, respectively. The dispersion relation of a transverse mode (TM or p-polarized) is given by[1,2]

$$\frac{k_x^2}{\varepsilon_{zz}} + \frac{k_y^2 + k_z^2}{\varepsilon_{xx}} = k_0^2, \tag{1}$$

where k_x, k_y, and k_z are the wavevector components in the x, y, and z directions, respectively; $k_0 = \omega/c$ is the incident wavevector; ω is the angular frequency of the incoming light; c is the speed of light in vacuum; and $\varepsilon_{xx}, \varepsilon_{yy} = \varepsilon_{zz}$ are the complex electric permittivities. More details of Eq. 1 can be found in section S1 of the Supporting Information (SI). Accounting for the signs of ε'_{xx}, ε'_{yy}, and ε'_{zz}, this dispersion relation forms a two-fold hyperboloid with an unbounded maximum magnitude of the propagating wavevector, $k = (k_x, k_y, k_z)$. Thus, high-k modes that are evanescent in optically isotropic materials can propagate in HMs.[1,2]

HMs capacity to support high-k waves has led to a variety of applications,[3–8] but of particular interest is their potential as infrared (IR) thermal emitters,[3,9–11] which leverage HMs' enhancement of the photonic density of states (PDOS) associated with large propogating k-vectors. An enhanced PDOS translates into higher spontaneous emission rates,[3,10] which make HMs operating in the IR ideal for thermophotovoltaic systems,[3,9–12] as they can induce stronger IR radiation emission into frequency bands suited to photovoltaics, a process holding promise, for example, to turn captured waste heat into electricity.

One commonly used technique for manufacturing HMs that exploit these unique properties is to place a metal between dielectric materials.[2] These artificial systems, referred to as hyperbolic metamaterials, can be hyperbolic at IR wavelengths. However, the largest propagating wavevector contributing to the PDOS enhancement is restricted by dissipation losses and, importantly, by the stacking periodicity of the medium (i.e., the bilayer thickness of a multilayer HM, which is the sum of the metallic and dielectric layer thicknesses).[11,13] In fact, for a HM to exhibit hyperbolicity, the material's effective permittivities should be homogeneous over the effective wavelength of a propagating mode, consistently with the effective medium approximation (EMA).[11,13,14] In formulae, this requirement reads

$$\left|\vec{k} \cdot \vec{d}_{\mathrm{c}}\right| \ll 1, \tag{2}$$

where $\vec{d}_{\mathrm{c}}$ is the system characteristic periodicity corresponding to the bilayer thickness in

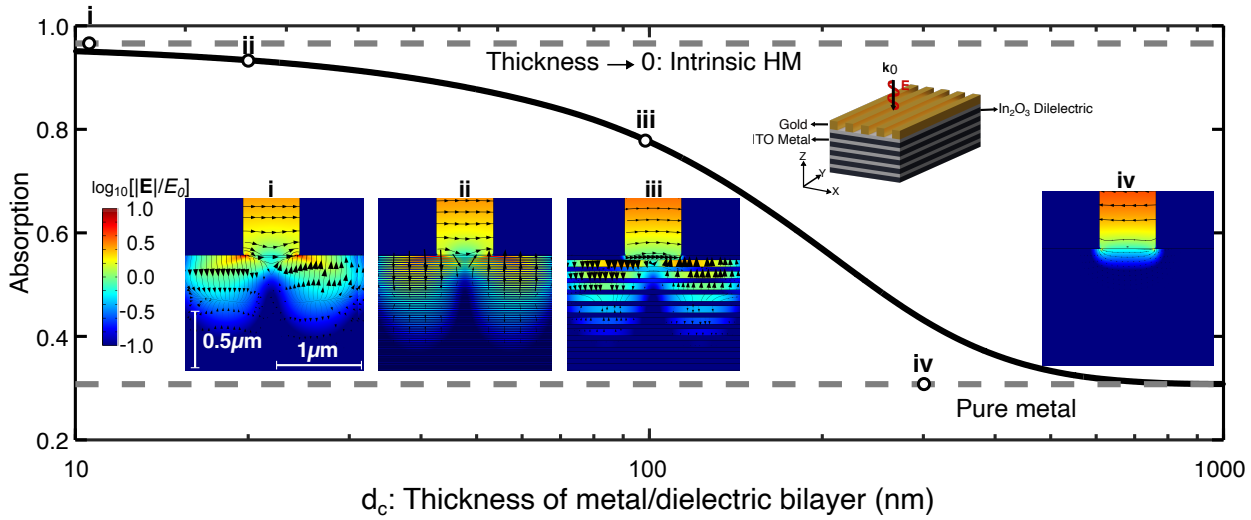

Figure 1: **Absorption characteristics of a Au-grating-coupled conventional hyperbolic metamaterial for different bilayer thicknesses.** Absorption of a Au-grating-coupled artificial HM at 1830 cm^{-1}.The four bottom insets show maps of the electric field (normalized to the input electric field E_0, in logarithmic scale) with the electric field vector (black arrows and streamlines) for various bilayer thicknesses. Top inset: Visualization of the materials and model used in the calculations. A plane wave at normal incidence (k_0 along the z-direction) with electric field polarized along the x-direction is considered. Note that the multilayer heterostructure here detailed is a uniaxial HM along the z-direction, i.e. $\varepsilon'_{zz} < 0$ and $\varepsilon'_{yy} = \varepsilon'_{xx} > 0$, differently from the case described by Eq. 1.

a multilayer HM (expressed as a vector to account for the direction of periodicity). If the homogeneity condition above is not satisfied, light does not interact with a properly defined hyperbolic medium, but rather with discrete metallic and dielectric regions.

To illustrate the limits of conventional hyperbolic metamaterials, we explicitly calculated the absorption of a multilayer HM with various thicknesses d_c, where absorption is defined as the integral of ohmic losses over the domain normalized to the incident power. The exemplary heterostructure considered consists of alternating layers of indium tin oxide (ITO) and indium (III) oxide (In_2O_3) placed below a gold diffraction grating (periodicity a = 2.0 μm) (top inset, Fig. 1). ITO+In_2O_3 is a low-loss hyperbolic metamaterial within the mid-IR,[15] and the gold diffraction grating is for coupling the free space incident radiation with the multilayer. We considered a normal incidence EM wave with exemplary wavenumber

$1/\lambda = 1830\,\mathrm{cm}^{-1}$ linearly polarized along the x-direction in calculating the absorption at various bilayer (ITO+In_2O_3) thicknesses, ranging from 10 nm to 1 µm, with the In_2O_3 layer thickness fixed at 1.5 times the thickness of the ITO layer (Fig. 1). More details are provided in SI Section S2.

For $d_c \geq 300\,\mathrm{nm}$, the multilayer HMs exhibits a minimal increase in absorption compared to a compact film of ITO, acting essentially as a pure metal (the bottom dotted gray line in Fig. 1). Conversely, for thicknesses between 300 nm and 50 nm, the system displays some enhancement in absorption, resulting from the excitation of so-called bulk plasmon polaritons (BPPs).[14,16–20] BPPs are high-k modes consisting of gap plasmons forming a bulk-like plasmonic excitation. Using the notations of Eq. 1, BPP modes travel almost exclusively along the metal-dielectric interfaces (x-direction),[19] with the electric field interacting through ε_{zz}. Non-BPP k-modes travelling along z, instead, rapidly decay as the imaginary part of the metallic permittivity typically dominates: $\varepsilon''_{xx} > \varepsilon''_{zz}$. As the bilayer thicknesses approach 50 nm, the absorption resembles intrinsic HM with vanishing d_c (Fig. 1.i).

From a fabrication standpoint, current thin-film deposition techniques can reach layer thicknesses as low as tens of nm.[16,20,21] However, reaching a small d_c is a major limitation when scaling a system's size for practical applications. To address this challenge, intrinsic HMs are often proposed: materials, such as bismuth, hexagonal boron nitride (hBN), V_2O_5, SiO_2 and many others[1,22], display virtually vanishing d_c, circumventing the need for precise top-down nanostructuring.[3,9,14] Additionally, the smaller d_c of these materials allows for the propagation of even higher-k modes, and accordingly, intrinsic HMs can exhibit fundamentally higher PDOSs than their artificial counterparts.

Unfortunately, many intrinsic HMs suffer from relatively narrow hyperbolic bandwidths,[1,22] especially in the IR region, limiting their use as broadband thermal emitters. To overcome such limitation, solutions have been proposed based on nanopatterning intrinsically anisotropic materials in order to achieve the photon-polariton momentum match. For instance, recent studies have reported promising enhanced performances of nanopatterned

hBN[23] and MoO_3[24,25] in the mid-IR and THz spectral region. One alternative approach relies on carbon nanotube (CNT) films. Aligning and packing CNTs produces artificial films which are hyperbolic over broadband IR frequency ranges,[9,26,27] and are thermally stable up to 1600 °C.[9] In particular, as we demonstrate below, macroscopic films of aligned and packed CNTs prepared via shear stress[28] are cost-effective and compatible with large-scale hyperbolic implementations, showing promise for the engineering of thermal emission platforms.

Manufacturing thick CNT films as, for example, thermal emitters is achievable; however, thick HMs (e.g., above ∼1 µm) display a limited interaction volume since absorption losses quickly quench modes traveling in the vertical direction (z). To enhance the interaction between light and scalable CNT-based hyperbolic emitters, a means for extending the optical excitation throughout the thickness of a HM is needed. In this work, we propose an emitter setup where a deep diffraction grating is etched directly into our hyperbolic material without an additional grating structure (such as the Au grating assumed above mentioned in Fig. 1). As such, the structure analysed follows the rationale of previous reports,[26,29] yet introduces the original aspect of having an anisotropic medium as both the grating and the material beneath it, promoting peculiar hyperbolic optical properties. In such a configuration, a gamut of electromagnetic modes can be in principle excited across the structure, encompassing (with more or less efficiency) surface plasmon polaritons, BPPs, and Rayleigh anomalies.[30] In addition, the deep grooves forming the grating act as Fabry-Pérot (FP) resonators and allow optical cavity modes to develop within the etched area, immediately surrounded by CNTs. This translates into the further excitation of confined hyperbolic plasmon modes (HPMs)[26,29] extending within the volume of the etched CNT antennas and guided in the (x) direction of periodicity of the grating, with properties derived from propagating HPMs. Importantly, these guided modes promote optical absorption over a broadband spectral region and enhance light-matter interactions across the hyperbolic medium considered. Once manufactured such a structure, more precisely consisting of an optically thick macroscopic

film of highly aligned and packed CNTs with the deep diffraction grating directly etched into the film, we experimentally characterized its optical properties, which are well reproduced by our finite element method (FEM) numerical simulations. We complemented the sample characterization with extensive FEM calculations to gain insight into the underlying optical phenomena. While some optical features are damped in current experimental conditions due to material losses, the theoretical analysis provides guidelines for future endeavors once more performing materials will become available. Special attention is given to FP-confined HPMs and their impact on the system optical response, revealing that these modes are, especially for thicker gratings, the primary contributor to the CNT film enhanced absorption and increased interaction with light. We predict that these confined modes are inherently related to the anisotropic nature of our hyperbolic CNT film (they cannot be excited across isotropic media) and exhibit deep sub-wavelength optical features which would be incompatible with more conventional (e.g. multilayer heterostructures) hyperbolic materials. We emphasize that such coupling is more practically attainable in intrinsic HMs due to the need for large grating thicknesses to support optical modes and the difficulty in obtaining them in hyperbolic metamaterials, highlighting aligned CNTs' promise as a new class of scalable IR hyperbolic materials.

Results and discussion

We prepared shear-stress-aligned CNT films[28] on glass substrates and transferred them to commercially available silicon substrates through a standard wet transfer technique. Our system is sketched in Fig. 2a, where the direction of tubes' alignment (i.e., the x-direction) is highlighted. The isofrequency contours of the corresponding dispersion relation (see Eq. 1) for the CNT-based artificial HM are depicted in Fig. 2b, while Fig. 2c shows optical and scanning electron microscope (SEM) images of the sample. See the Methods section for more details on the fabrication and wet transfer processes. The alignment of CNTs can be

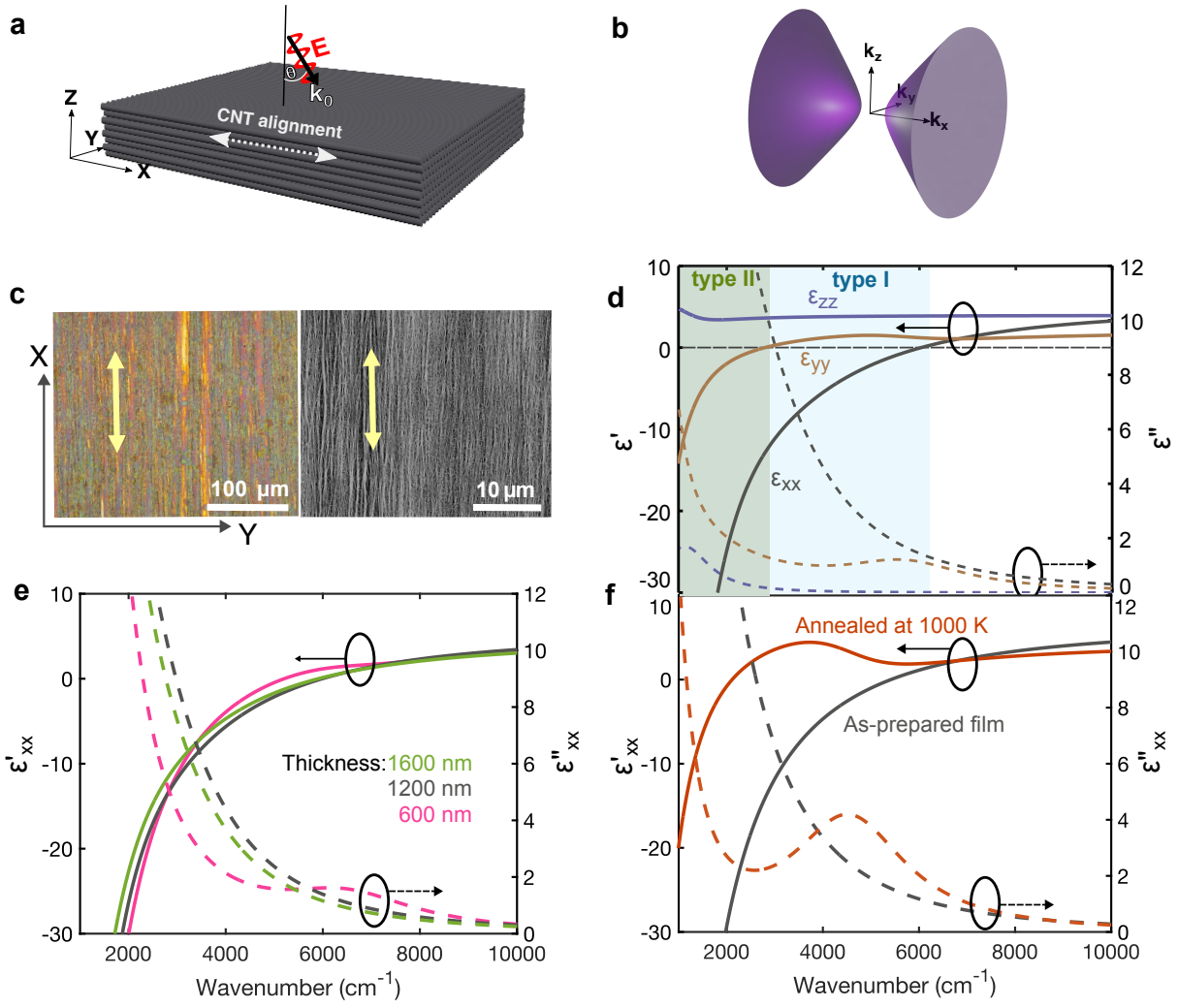

Figure 2: **Characterization of wafer-scale aligned CNT films**. a) Schematic of the hyperbolic film of aligned carbon nanotubes (CNTs) under investigation. (b) Visualization of the isofrequency contour of the CNT film hyperbolic dispersion relation. (c) An optical microscope image and a scanning electron micrograph of an aligned CNT film prepared by the shear-stress method. (d) The real (solid) and imaginary (dashed) dielectric constants of 1.2 μm thick CNT film along the x, y, and z directions (inset), with regions of optical hyperbolicity of type I (II) shaded light blue (green). (e) ε_{xx} for aligned CNT films with varied thicknesses. (f) Dielectric constants of as-prepared and annealed (at 1000 K) aligned CNT films, displaying de-doping effects.[26]

observed at both low and high magnifications (Fig. 2c, left and right panels, respectively). In both images, it can be seen that the wafer-scale aligned CNT film is dense and uniform, with the average diameter of CNTs being 1.8 nm.[31]

We conducted zero-order reflection and transmission spectroscopy measurements on the

obtained CNT film at various angles of incidence, both in TM and TE polarizations (see inset, Fig. 2a), and extracted the permittivity tensor ε_{xx}, ε_{yy}, and ε_{zz} from those measurements (where x is the alignment direction, as indicated by Fig. 2a, Fig. 2c). We assumed a Drude–Lorentz model for the permittivity functions, evaluating the fit by comparing calculated reflection and transmission spectra with the experimental measurements. Figure 2d shows the dielectric functions extracted from the experimentally measured reflection spectra, which are highly anisotropic, including in the xy-plane (see Fig. S3a, Fig. S3b, reporting polarization-resolved measurements along the x and y-direction, before and after etching). ε'_{xx} is negative for wavelengths longer than 1.6 µm (shaded blue in Fig. 2d), while ε'_{zz} remains positive over the entire spectrum under consideration. This ultra-broadband hyperbolic dispersion is absent in many intrinsic HMs operating in the IR.[1,22]

Note that in an ideal, perfectly aligned CNT film, one expects that $\varepsilon_{xx} < 0$ and $\varepsilon_{yy} = \varepsilon_{zz} > 0$, as in type I in-plane HMs.[23,32,33] However, there is a deviation between ε_{yy} and ε_{zz} as retrieved by our Drude fit, resulting into an anisotropy in the zy-plane (as ascertained experimentally, see Fig. S3c). Moreover, note that by fitting our reflectivity measurements we also predict $\varepsilon_{yy} < 0$ below 2500 cm^{-1}. As such, in this spectral region, our artificial CNT-based HM becomes a type II out-of-plane HM, as, e.g., hBN[34]. We explain this by observing that the shear-stress-assisted alignment technique can lead to nearly perfect alignment in the x–z plane whereas a certain amount of misalignment can arise in the y–x plane,[28,35] lending an additional metallic characteristic to ε_{yy}. This hyperbolicity-type transition, making our CNT film particularly intriguing as a new platform compared to other hyperbolic media, is however not explored in the present work (the light beams used are polarized in the xz-plane and do not experience ε_{yy}), and it will be the subject of future studies. Besides this peculiar behaviour in the y-direction, the film remains strongly hyperbolic within the mid-IR and long-wavelength IR, provided that the light source has some polarization in z. The imaginary permittivity of our CNT film, ε'', is also shown in Fig. 2b. ε'' is on the same order or smaller compared with other hyperbolic metamaterials,[7,20,36] given that

the largest imaginary dielectric constant, ε''_{xx}, is only about 12 around 2800 cm^{-1}, and 1.5 near the epsilon near zero (ENZ) point, where ε'_{xx} crosses zero at 6000 cm^{-1} (defining the plasma frequency). Conventional hyperbolic metamaterials often suffer from large ε'', due to ohmic losses in the metals they comprise. The acceptable ε'' of the aligned CNT film further emphasizes its utility as an intrinsic HM, as quenching high k-modes in the CNT film is more challenging.

To determine the impact of the film thickness on the dielectric constants, we analyzed the optical properties of aligned CNT films with varying thicknesses, from 0.6 µm up to 1.6 µm. The extracted optical constants for three different thicknesses are presented in Fig. 2e. The observed deviation in ε_{xx} for different film thicknesses is smaller than the accuracy of our extraction procedure. Thus, we conclude that the shear-stress alignment method can produce thick films of aligned CNTs with no appreciable misalignment in z, given an appropriate amount of time to stack aligned layers is taken.

We also studied the samples' refractory properties in line with a previous study focused on aligned CNTs' potential as IR thermal emitters.[9] In Fig. 2f, we compare the ε_{xx} of an as-prepared CNT film against an annealed CNT film. Annealing was carried out in a vacuum chamber at 1000 K for one hour. A significant lowering of the plasma frequency is observed, with the ENZ frequency dropping from 6000 cm^{-1} to 2000 cm^{-1} (compare red curves in Fig. 2f). Note that, likewise, annealing alters the dielectric constants in the other, y- and z-directions as well (see Fig. S4). Previous reports have shown that high-temperature annealing causes de-doping of CNTs, irrespective of the alignment method used, which thus lowers the plasma frequency.[9,26] However, once annealed, the optical constants of the films remained stable at high temperatures, confirming aligned-CNT films' potential as a refractory hyperbolic material platform.

To couple light from air into the CNT film and excite confined EM modes within the textured HM, we etched a diffraction grating into the surface of the film itself . Figure 3a shows the fabrication steps and scanning electron micrograph of the CNT film with an

etched diffraction grating, with Fig. 3b showing zero-order reflection spectra for the etched and unetched films measured with a Fourier-transform IR spectrometer.

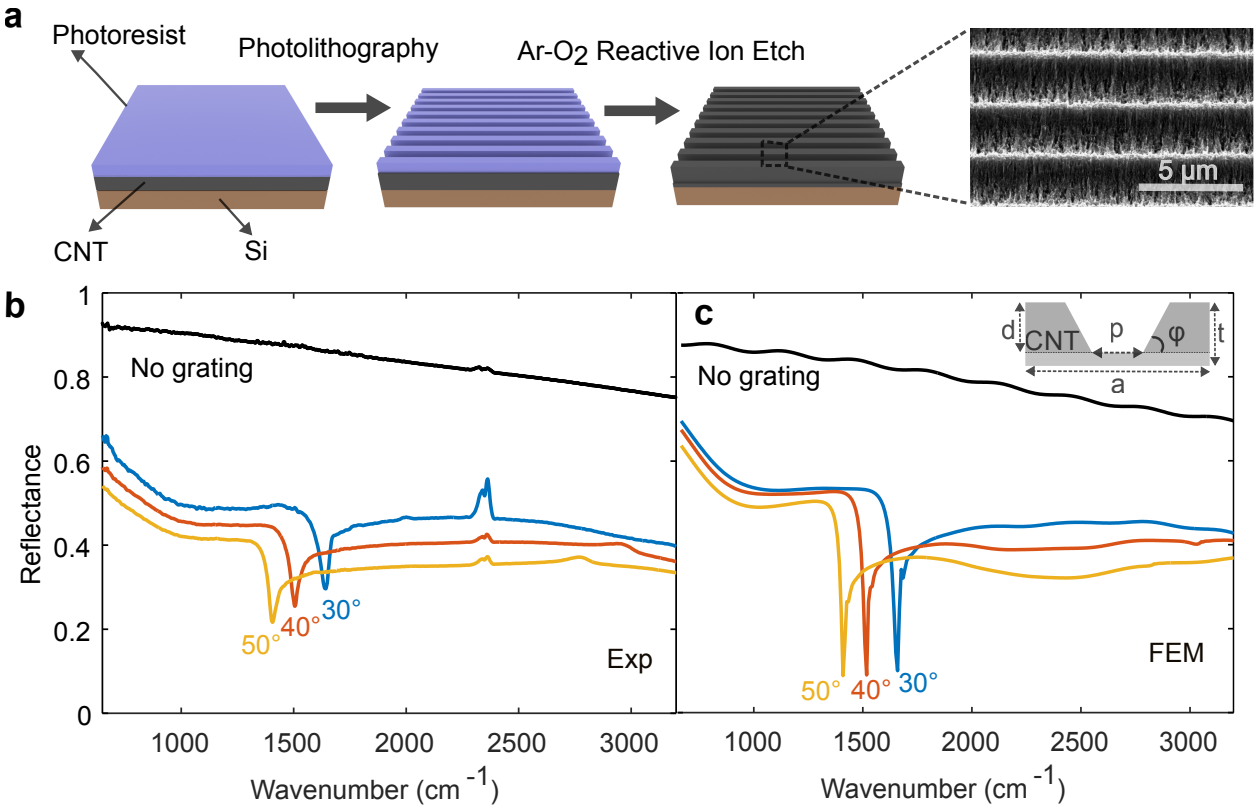

Figure 3: **Reflection measurements of a 0.4 µm-thick CNT film with a grating.** (a) Fabrication steps and a scanning electron micrograph of the 1D diffraction grating etched onto aligned CNT film. (b) Measured and (c) calculated (FEM) reflection spectra for a flat CNT film and a CNT film with an etched diffraction grating (total thickness $t = 1.2\,\mu$m, periodicity $a = 4.0\,\mu$m, etched width $p = 1.6\,\mu$m, and grating slope $\varphi = 27°$) perpendicular to the direction of CNT alignment, at different angles of incidence, θ. In all measurements, the electric field was polarized in the x–z plane (see inset of Fig.2b).

The reflectance of films with gratings is much lower than unetched films over a broad IR spectrum and presents some (albeit relatively shallow) resonant features absent otherwise, as can be seen by comparing the spectra of films with and without the etched diffraction grating, in Fig. 3b. This confirms the role of the grating in enabling to excite modes across the structure upon illumination from air. The specific physical mechanism behind such grating contribution depends on the mode analyzed, and results from the combination of periodicity, thickness and filling fraction (void-to-material ratio)

In particular, by inspecting Fig. 3b, a sharp dip in reflection arises (at $\sim$ 1400 cm^{-1} for $\theta = 50°$, yellow curve, and reaching 1700 cm^{-1} for $\theta = 30°$, blue curve), dominating the system's spectral response. This feature (together with the smaller peaks observed at around 2700 cm^{-1}) closely corresponds to a predicted surface plasmon polariton (SPP). SPPs are EM excitations at a metal-dielectric interface and display a locally enhanced electric field. The metallic character of ε_{xx} allows for propagating SPPs in x, along the interface between the environment (air) and the grating, and the grating serves to provide the extra k_x component required to fulfill the phase matching condition and launch the surface wave (see SI section S5). Our interpretation is corroborated by analytical calculations of the SPP dispersion relation (see Fig. S5), as well as further supported by the observed dispersive behaviour of the mode as a function of the angle of incidence (the peak red-shifts when increasing the incidence angle).[37]

Besides SPPs, some additional features are present, yet less pronounced, in the measured spectra, including a (rather shallow, due to the specific sample employed) dip at 1000 cm^{-1}, that, with the aid of numerical simulations, we interpreted as a confined hyperbolic plasmon mode mediated by the Fabry-Pérot resonators composing the grating. For this interpretation and, more generally, for an in-depth understanding of the mechanisms behind the features in the CNT optical spectra, we performed extensive FEM-based numerical calculations. We began by comparing the measured reflection in Fig. 2b with simulations performed on the experimental geometry with the optical constants extracted from fits, as shown in Fig. 3c. The calculated reflection spectrum exhibits excellent agreement with experimental measurements, with slight discrepancies attributed to fabrication imperfections (in particular, the peaks at 2300 cm^{-1} are attributed to a measurement artifact caused by slight changes in atmospheric CO_2 level between sample and reference measurements).

Then, to disentangle more clearly the physical mechanisms underlying the reflection spectra in Fig. 3c, we gradually modified the numerical model by altering the geometry and optical properties to assess their impact on the system. This step-by-step computational

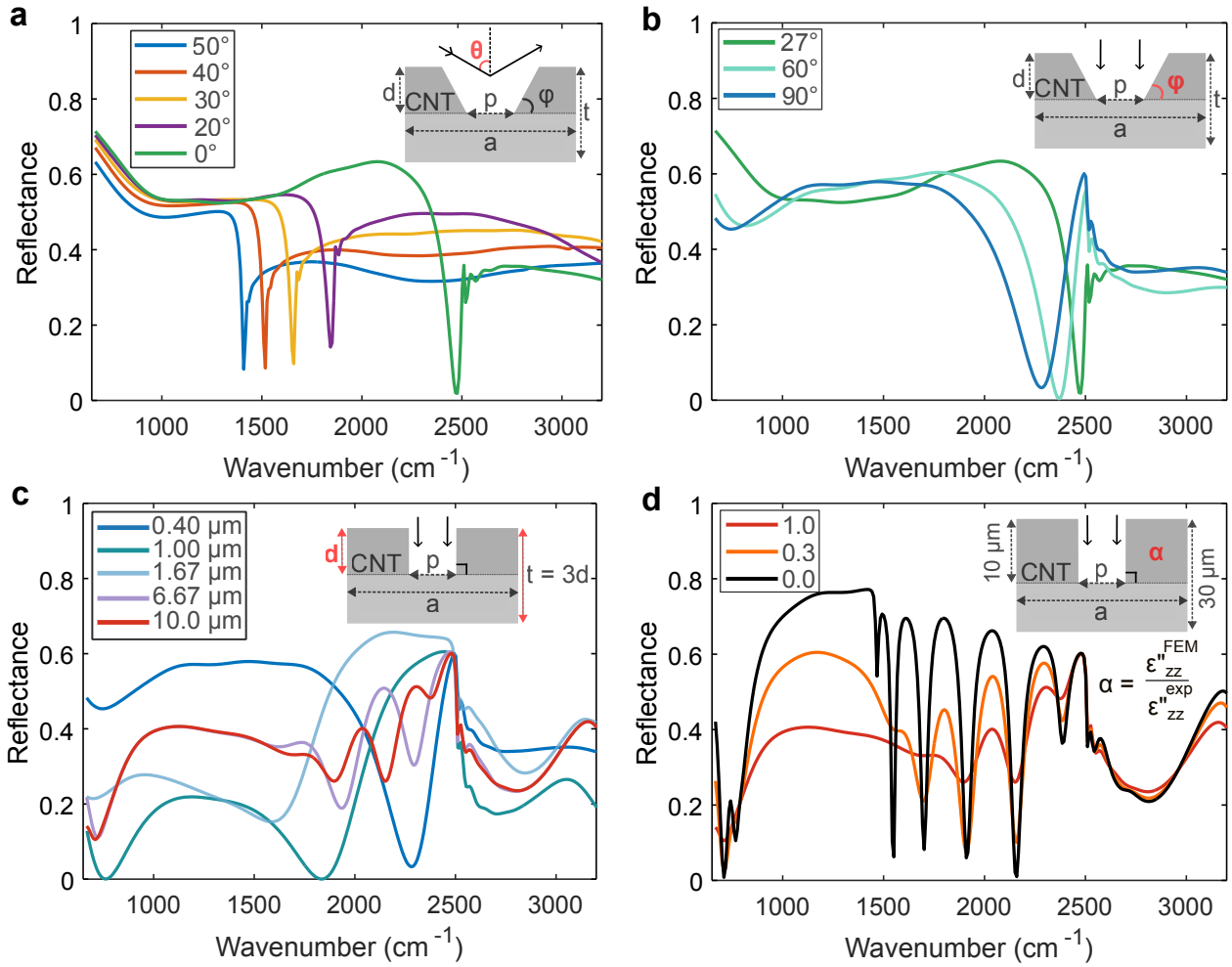

Figure 4: **Transition from experimental to ideal geometry in FEM calculations.** In each of the sub-figures, the variable highlighted in red in the inset is swept, while the other variables are kept fixed from the previous set of calculations. In all calculations, $a = 4.0\,\mu\text{m}$, $p = 1.6\,\mu\text{m}$, and $t = 3d$. (a) The angle of incidence (θ) is varied from 50° to 0°. (b) The slope of the diffraction grating (φ) is swept from the experimentally etched grating (27°) to an ideal rectangular grating (90°). (c) Thickness d of the CNT grating is increased from 0.4 μm to 10 μm, with $t = 3d$. (d) ε''^{FEM}_{zz} is proportionally lowered from the experimentally determined value ($\alpha = 1$) to zero ($\alpha = 0$), where $\varepsilon''^{\text{exp}}_{zz}$ is the imaginary permittivity in z measured in experiments, and $\varepsilon''^{\text{FEM}}_{zz}$ is the imaginary permittivity in z used for the calculations.

tuning allowed us to identify the optical phenomena at play, providing further guidelines for future fabrication efforts. Special attention was given to confined HPMs, i.e. the dips observed experimentally (Fig. 3b) around 1000 cm^{-1}. Section S6 in the SI reports on a detailed numerical analysis of the evolution of the mode associated with such experimental dip upon the parameters variations considered in the following, and it further elucidates the

character of this mode. We began by decreasing the angle of incidence of the driving EM source from 50° to 0° (as depicted by the blue and green curves in Fig. 4a, respectively) keeping all other parameters fixed, which has, as expected, the major effect of blue shifting the SPP. Note that the diffraction grating contributes momentum in the $+x$ and the $-x$ directions (see Eq. S6 in the SI), resulting in two distinct coupling conditions for guided modes.[38] Forcing $\theta = 0°$ makes both contributions degenerate, enhancing the overall coupling strength and making the spectra simpler to analyze.

Next, we increased φ, the interior angle of the etched diffraction grating from the experimental 27° to the ideal rectangular 90°, as shown in Fig. 4b. This modification red-shifts the local zeroth-order reflection minima of the green $\varphi = 27°$ curve and aids in separating spectrally a dip in reflectance, related to SPP excitation, and a (slightly blue-shifted) peak, falling precisely at the inverse of the grating period (2500 cm^{-1} for a 4 µm pitch) for the three configurations and ascribed to a Rayleigh anomaly (i.e., diffraction parallel to the grating). Furthermore, at smaller wavenumbers, the shallow dip originally sitting around 1000 cm^{-1} and interpreted as the lowest-order HPM confined within the FP resonator red-shifts and gets more pronounced. Such trend is rationalized by the fact that straightening the walls of the etched air cavity decreases scattering, and promotes the formation of optical modes related to the excitation of resonators across the grating. Higher-order FP resonances are instead expected to fall close to the SPP, making it hard to distinctly resolve them.

Then, we increased d, the thickness of a rectangular $\varphi = 90°$ diffraction grating, from 0.4 µm to 10 µm, as shown by Fig. 4c. Overall, increasing the grating thickness makes the simulated spectra richer. More in detail for what pertains to the confined HPM modes, at low wavenumbers, the dip red-shifts and significantly drops, by decreasing from ∼50% to below 20% for all curves. Moreover, as the thickness continues to increase, the number of dips across the spectrum increases, as thicker diffraction gratings allow higher-order optical cavity modes to develop within the etched cavity (the number of modes allowed increases in the direction of the groove height, see also SI section S6). The spatial patterns of such

modes are highly localized within the antennas making up the grating, offering more efficient coupling between the incoming radiation and the FP-confined HPMs. This promotes higher absorption compared their thinner counterparts, mostly featuring surface modes, as illustrated in Fig. S9. Note that a further relevant geometrical parameter that can be changed is the grating period. Reducing the periodicity up to the limit of having a deep subwavelength grating, thus transitioning into the regime of metamaterial, enables much stronger confinement factors, highly desirable for the study of hyperbolic polaritons.[23] The effects of employing a decreased periodicity for our specific system are detailed in Fig. S14 and S15.

Overall, the various EM modes across the structure, and especially confined HPMs, are still hindered by losses, that eventually quench their excitation. To better access these modes' contribution, we thus reduced absorption for z-polarized propagating modes along the metallic direction, allowing for a more in-depth analysis of each mode. In essence, artificially reducing losses of the anisotropic system metallic component brings our observation much closer to what is commonly observed for hyperbolic phonon polaritons, where the losses are intrinsically lower.[23,39,40] Figure 4d details the effects of lowering $\alpha = \varepsilon''^{\mathrm{FEM}}_{zz}/\varepsilon''^{\mathrm{exp}}_{zz}$ on the reflection spectrum, which in turn promotes the formation of HPMs within the grating FP resonators in our calculations, revealing several new minima in reflection.

In addition to confined HPMs, having a low-loss material enables in principle to excite also BPPs across our system. Simulations revealed their presence, showing how in fact, even assuming reduced losses, they carry a relatively small amount of power in the specific case under scrutiny, which hindered to measure them in our experimental conditions. More details are provided in SI section S7.

We provide further insight into the mechanisms of coupling optical cavity modes to the HM via confined HPMs in Fig. 5, which compares the case where a diffraction grating is directly etched into a hyperbolic aligned CNT film with the case of an external diffraction grating placed on top of the CNT film. The absorption spectrum of a CNT grating and an exterior gold grating, with various grating thicknesses, is shown in Fig. 5a. Absorption is

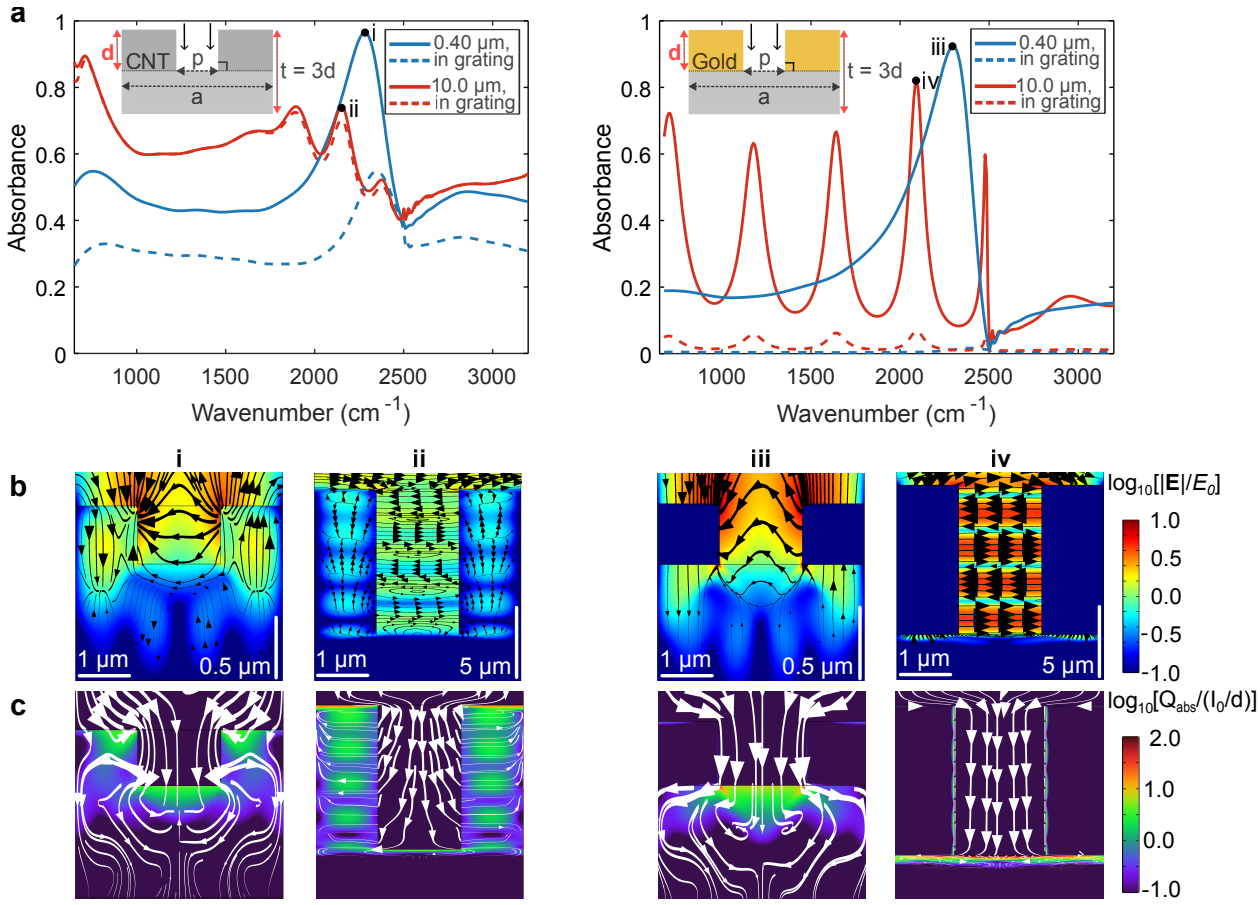

Figure 5: **HM grating compared to gold grating, over various thicknesses.** In all calculations, $a = 4.0\,\mu\text{m}$, $p = 1.6\,\mu\text{m}$, and $t = 3d$. (a) Absorption spectrum for light coupled via a diffraction grating composed of aligned CNT, and a diffraction grating composed of gold. Dashed lines represent absorption solely in the diffraction grating. (b) Logarithmic electric field (normalized to the input electric field), with the electric field vectors, and (c) logarithmic absorption map (normalized to the input intensity over d), with Poynting vectors, for the wavenumbers and thickness specified in (a).

calculated directly from resistive losses in the medium

A local maximum in absorption occurs at $2300\,\text{cm}^{-1}$ for $d = 0.4\,\mu\text{m}$ in the gold grating (labelled iii), with a similar excitation occurring at $2280\,\text{cm}^{-1}$ for the aligned CNT grating (labelled i). Comparing the electric field maps in Fig. 5b and the absorption maps of Fig. 5c suggests that the two modes are optically similar. We relate this resonant feature to a SPP excitation, with the grating providing the additional momentum contribution to launch the surface wave, regardless of its optical, either hyperbolic (aligned CNTs) or isotropic (pure metal, Au), character.

The most distinct difference between the behavior of the gold and CNT gratings is how they interact with optical excitations in the antennas, that, in the latter case, are made of a hyperbolic medium instead of an isotropic metal. The CNT grating couples these excitations via polaritonic FP resonances directly into the grating, forming cavity modes within the grooves volume, as shown by the electric field maps of Fig. 5b.ii. Conversely, the Au grating rather locally enhances the incident field within the gap region, i.e. in the air between nearest grooves, with a negligible portion of both field and dissipated power concentrated inside the grating antennas (Fig. 5b.iv). Although using a CNT grating does not necessary lead to an overall increase in absorption at the confined HPMs (even if its absorption is substantially increased over a broadband spectrum), coupling optical modes into a hyperbolic grating extends the excitation throughout the grating thickness, exciting deeper regions of the HM than via grating coupling (Au grooves on HM) alone.

Further analysis of the absorption spectrum for the $\alpha = 0$ case (black curve in Fig. 4d) was performed, aiming to investigate the main characteristics of the polaritonic FP resonances supported by our simulated system (in the ideal conditions of absence of losses). These modes arise indeed from a rather complex interplay of contributions coming at the same time from the individual groove antennas (the width and thickness of which are both relevant in exciting FP-like resonances), the grating configuration (resonances are not insensitive e.g. to variations of the grating periodicity, see SI section S6, although they can be excited also by single antennas, contrary e.g. to SPPs), the compact CNT layer beneath the grating, and the anisotropic optical properties of the material (both in the etched and the compact regions). Previous reports[26,29] have detailed these modes' hyperbolic dispersion and great potential in localizing light to extreme sub-wavelength dimensions, yet by considering arrays of hyperbolic resonators on a dielectric, isotropic substrate. In parallel, in the presence of high contrast gratings, a more complex phenomenology of resonances can arise in terms of guided-mode anomalies, considering that a dielectric film on top of a hyperbolic substrate can support guiding effects beyond the trivial condition provided by conventional all-dielectric systems.[41]

These studies partially corroborate our analysis, although the exact same treatment they report does not apply to our peculiar system, which has not been fully detailed yet in the literature. A holistic and more general understanding of the modes supported by a hyperbolic grating lying on a hyperbolic substrate as our sample falls out of the scopes of the present work, and will be the subject of future, dedicated studies. For our analysis, the absorption spectrum of Fig. 4d is examined in depth in Fig. 6a, alongside the normalized electric field amplitudes and directions (Fig. 6b), and normalized maps of absorption with Poynting vector (Fig. 6c) evaluated at relevant frequencies over the calculated spectrum.

To refer to the observed HPMs more exhaustively, we labelled them in terms of n, representing the mode order (i.e. number of nodes of the electric field) along the x, horizontal direction, and m, numbering instead the FP order in the z, vertical direction. Refer also to SI section S6 for further details.

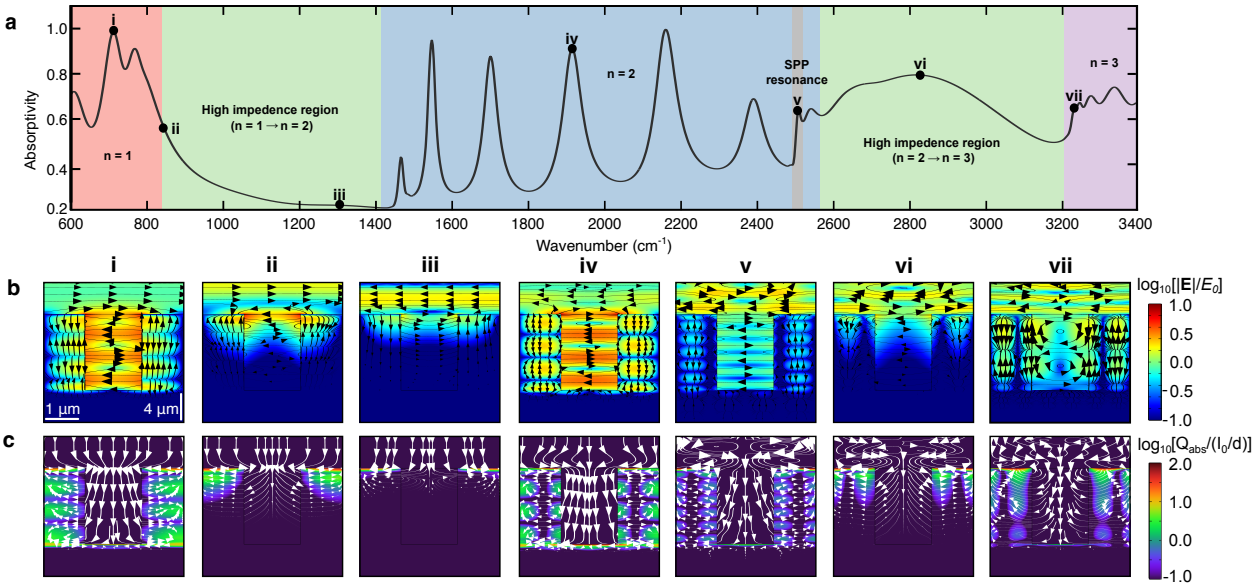

Figure 6: **Detailed analysis of confined HPMs in the lossless regime** (a) The absorption spectrum of the CNT diffraction grating. For the specified frequencies: (b) the logarithmic electric field (normalized to the input electric field) with electric field vectors, (c) the logarithmic absorption map (normalized to the input intensity over d) with Poynting vectors. Specified wavenumbers correspond to: i) the $|n| = 1$, $|m| = 4$ FP antenna mode; ii) the transition to higher n-order FP resonances; iii) the lowest absorption frequency; iv) the $|n| = 2$, $|m| = 4$ FP mode; v) the SPP resonance; vi) the transition to higher n-order FP resonance vii) the $|m| = 1$ FP mode for $|n| = 3$.

The $n = 1$ region of Fig. 6a displays three distinct peaks, linked to the $|n| = 1$, $|m| = 3, 4, 5$ modes. As expected from the inherent confinement effect required to support them, peaks in absorption due to FP-like resonances occur when the optical antenna excitation is extended into the grating. Indeed, the electric field computed for these frequencies is highly localised within the grooves volume. Likewise, the Poynting vector field in Fig. 6c.i exhibits a significant magnitude in the cavity between grooves, from where it enters the grating with high efficiency and promotes light absorption. As the frequency increases, the coupling with the grating antennas becomes weaker, and the incident light penetration within the HM is hindered. The corresponding fields (Fig. 6b.ii) get mostly localised at the top of the grating, up to the case where almost no coupling is observed (Fig. 6b.iii). This would explain the drop in absorption and increased reflection, in the transition, high-impedence region that does not support FP-like HPM excitation. However, at larger frequencies, light can again couple into the HM via FP resonances in the grating grooves. This corresponds to the set of modes featuring 2 nodes (hence 3 lobes) in the x direction within the antennas, although the transition in n is not sharp (the first peaks observed in the $n = 2$ region are associated with non-zero fields at the air/groove interface). Overall, the $|n| = 2$ FP modes behave essentially in the same way as the previous set, with peaks in absorption linked to optical modes coupled into the CNT grating and electric field patterns exhibiting an increasing number of lobes in the vertical direction, corresponding to allowed FP solutions in the resonating antennas. Moreover, overlapping with this spectral region, the SPP can be excited (Fig. 6b.v). Note that the plasmonic peak, one of the core features of the experimental spectrum in Fig. 3, is now a minor feature of Fig. 6a. This is partly due to eliminating losses of light propagating along x; however, it is the magnitude of the optical modes within the cavity that makes the SPP mode a relatively minor feature, as shown in Fig. 4. Despite the lack of FP modes, significant, broadband absorption in the CNT film is present in the second transition region. Even with a relatively high absorption, any resonant feature is substantially lost, and the fields remain localised at the antenna top surface (Fig. 6b.vi). Then, at $3200\,\mathrm{cm}^{-1}$, the $|n| = 3$

FP resonances region begins and extends through the rest of the analyzed spectrum. Again, the predicted modes behave similarly to the $|n| = 1, 2$ ones, as shown for the exemplary case of the $|m| = 2$ mode pictured by Fig. 6.vii.

Overall our analysis shows how the interplay between confining antennas and otherwise propagating hyperbolic modes can generate large absorption within the cavity volumes formed by the grating grooves. This confinement of high absorption regions in the outermost domains of a HM film can be relevant for studying surface effects and molecular interactions where the co-localization of input radiation, carrier generation and photothermal effects is beneficial.[42–44] Further work will be devoted to the realization of even thicker gratings to exploit the potential of highly absorptive FP modes in HMs.

Conclusion

Owing to an enhanced photonic density of states, macroscopic hyperbolic films are more efficient in absorbing and emitting light than conventional isotropic materials. We manufactured and characterized a unique structure consisting of an optically thick wafer-scale film of highly aligned and packed CNTs with a deep diffraction grating directly etched into the film. The hyperbolic dispersion and ease of manufacturing of this architecture make it a good candidate for constructing future IR hyperbolic materials and devices for various applications. Using experimental measurements and full-wave numerical calculations, we explored ways to enhance the aligned CNT film's absorbing/emitting efficiency, optimizing the geometrical and optical parameters to maximize the film's performance over a broadband range in the mid-IR.

We demonstrated that optical absorption within this novel hyperbolic structure is enhanced when optical cavity modes couple with FP resonances across the hyperbolic grating antennas, thus confining hyperbolic polariton modes otherwise propagating. Our numerical study opens to more focused and extensive analyses on the promising optical properties of

hyperbolic gratings lying directly on a hyperbolic medium, towards the engineering of desired properties for specific photonic applications.

This work indicates that thick aligned CNT films prepared by the shear-stress method are uniquely positioned to take advantage of these confined cavity modes, requiring little manufacturing or correction to retain a hyperbolic dispersion at the macroscopic scale. Consequentially, aligned CNT films are a natural candidate for future thermal emitters exploiting the enhanced spontaneous emission rate of HMs.

Methods

Preparation of aligned CNT films by the shear-stress method

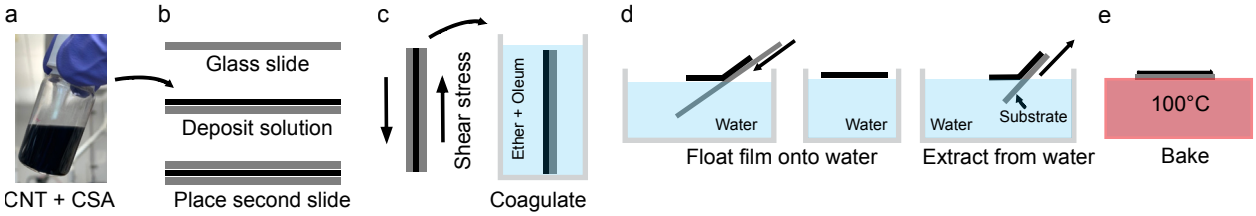

Figure 7: **Preparation of aligned carbon nanotube films by the shear-stress method.** Schematic showing details of the shear-stress alignment technique and wet transfer process employed to fabricate aligned CNT films.[28] a) Dissolution of CNTs in CSA. b) Transfer of the CNT+CSA solution to glass slides. c) Application of shear stress alignment, and transfer to an ether + oleum coagulate. d) Extrationg of CNT films from the glass slide and transfer to a substrate. e) Drying of the CNT film.

Aligned CNT films are fabricated following a procedure used by Headrick et al.[28] CNTs (Meijo NanoCarbon) are dissolved in chlorosulfonic acid (99%, Sigma) and mixed until a homogeneous solution is formed (see Fig. 7a). A small quantity of the solution is transferred to a glass slide, and then sandwiched another glass slide. Afterwards, the slides are pressed together to evacuate air bubbles (see Fig. 7b). The slides are then sheared apart in the long direction, and placed in a coagulant of diethyl ether (Fisher) and fuming sulfuric acid (120%, Alfa Aesar) (see Fig. 7c). This mixture extracts the CSA acid solvent and solidifies the CNTs on the surface of the glass slides, locking in the orientation developed during shear.

The slides are removed after 30 seconds. To separate the CNT films from the glass slide, the slide is inserted at a small angle into a water bath such that the CNT film floats onto the water surface. The Si substrate (UniversityWafer, Inc) is inserted into the water bath and then removed vertically upward in such a way that the film is positioned in the desired orientation on the substrate (see Fig. 7d). The sample is then dried on a hotplate at 100 °C for 1 hour (see Fig. 7e)

Fabrication of gratings on CNT films

We used standard photolithography technique to define large area grating pattern on as-prepared samples. a positive photoresist (Microposit-S1818) was used both for patterning and as an etch mask. After patterning, the grating structure was etched employing a reactive ion etch (Oxford, Plasmalab System 100/ICP180) with a mixture Ar and O_2 gases at flow rates of 50 and 10 sccm, respectively. The capacitively and inductively coupled RF powers were maintained at 50W and 250W, respectively. We used a Bruker Multimode 8 atomic force microscope (AFM) to determine the thickness of CNT films and grating profile.

Measurements

All reflection measurements were carried out using a Fourier-transform IR spectrometer (Thermo Fischer Scientific, iS50R) equipped with a variable angle specular reflection accessory (PIKE technologies, VEEMAX III). A gold mirror was used as the reference to measure absolute reflectivity of CNT films and gratings.

Simulation methods

Numerical calculations were carried out using a FEM-based commercial software (COMSOL version 6.0). Maxwell's equations are solved across a unit cell of the analyzed material, with Floquet boundary conditions used to simulate an infinite periodic array. For Figure 1, a 1 µm

gold diffraction grating on a 2 µm thick layer is simulated. The optical constants of gold are taken from ref.[45] A 15 µm-thick layer of air (refractive index equal to 1) is placed above the gold diffraction grating, and a 3 µm-thick Perfectly Matched Layer (PML) defined on top of the physical air domain to avoid spurious reflections. A periodic port at the air domain's top boundary provides the wave excitation. An in-plane linearly polarised plane wave is simulated, with the corresponding magnetic field polarized along the y direction, impinging on the structure with angle of incidence $\theta = 0°$. The grating and analyzed material lies on a a 5.0 µm-thick substrate made of amorphous silicon, with a 0.86 µm PML below the substrate. The optical constants of Si are taken from Chandler et al.[46] A periodic port sitting above the PML layer tracks light that penetrates through the film, although in practice, transmission is negligible in all calculations.

For most calculations, the 2 µm film of analyzed material consists of ITO+In_2O_3 layers, spanning 2 to 200 bilayers. Optical constants for ITO and In_2O_3 were taken from a Drude fit specified by Guo et al.[15] Layer counts 2-10 were compared against a 10 µm thick HM layer with an identical layer thicknesses, to ensure the lower layer count had minimal impact on the absorption spectrum; no significant deviations are noted.

The intrinsic HM absorption of Figure 1c.i was calculated by passing the effective dielectric constants for Figure 1c to a single, uninterrupted 2 µm layer, simulating a material with infinitely thin bilayer thickness. The ITO layer of Fig. 1c.iv was simulated using the dielectric constants of ITO on a 2 µm block of ITO underneath the grating.

A free-triangular-element mesh was used within the physical domain of the simulation, with a maximum element size of 0.33 µm in air, 0.09 µm in the substrate, and 0.017 µm in the Gold grating. Individual films were meshed with a size of 0.017 µm or a quarter of the thickness of the layer, whichever was smaller.

Analysis with CNT proceeded similar, with the same channel of air, the same substrate (both backed by a PML), the same Floquet periodic boundary conditions, and the same exciting periodic port. The free tetrahedral mesh size of aligned CNT is set to 0.033 µm in

all calculations.

Supporting Information Available

The following Supporting Information is available free of charge at the ACS website:

> Dispersion relation derivation; Dielectric constants of ITO+In_2O_3; Optical anisotropy in aligned CNT films; Effect of annealing on CNT optical constants; Surface plasmon polaritons (SPP); Confined hyperbolic plasmon modes in CNT Fabry-Pérot nanoresonators upon variations of the experimental geometry; Plasmon polaritons (PPs) in the CNT film and their dispersion: bulk and surface PPs.

Funding Sources

B.J. acknowledges support from the Ken Kennedy Institute of Computational Science and Engineering Recruiting, funded by the Rice Oil & Gas HPC Conference.

A.S. and G.D.V. acknowledge support from the METAFAST project that received funding from the European Union Horizon 2020 Research and Innovation programme under Grant Agreement No. 899673. This work reflects only author view and the European Commission is not responsible for any use that may be made of the information it contains.

J.D., A.B., and J.K. acknowledge support from the Robert A. Welch Foundation through grant number C-1509, the Air Force Office of Scientific Research through grant number FA9550-22-1-0382, the JST CREST program, Japan, through grant number JPMJCR17I5, the US National Science Foundation through grant number PIRE-2230727, and the Carbon Hub of Rice University, and the Chan–Zuckerberg Initiative (CZI) through grant number 2020-225832.

J.K. acknowledges support from the Robert A. Welch Foundation through grant number C-1509, the JST CREST program, Japan, through grant number JPMJCR17I5, the US

National Science Foundation through grant number PIRE-2230727,

J.K. and G.N. acknowledge the support of the Carbon Hub of Rice University

O.S.D. and M.P. acknowledge the support of Department of Energy (DOE) award DE-AR0001015 (Advanced Research Projects Agency–Energy).

References

(1) Shekhar, P.; Atkinson, J.; Jacob, Z. Hyperbolic metamaterials: fundamentals and applications. *Nano convergence* **2014**, *1*, 1–17.

(2) Poddubny, A.; Iorsh, I.; Belov, P.; Kivshar, Y. Hyperbolic metamaterials. *Nature Photonics* **2013**, *7*, 948–957.

(3) Lee, D.; So, S.; Hu, G.; Kim, M.; Badloe, T.; Cho, H.; Kim, J.; Kim, H.; Qiu, C.-W.; Rho, J. Hyperbolic metamaterials: fusing artificial structures to natural 2D materials. *ELight* **2022**, *2*, 1–23.

(4) Pendry, J. B. Negative refraction makes a perfect lens. *Physical review letters* **2000**, *85*, 3966.

(5) Kim, Y.; Lee, G.-Y.; Sung, J.; Jang, J.; Lee, B. Spiral metalens for phase contrast imaging. *Advanced Functional Materials* **2022**, *32*, 2106050.

(6) Messina, R.; Ben-Abdallah, P.; Guizal, B.; Antezza, M.; Biehs, S.-A. Hyperbolic waveguide for long-distance transport of near-field heat flux. *Physical Review B* **2016**, *94*, 104301.

(7) Sreekanth, K. V.; Mahalakshmi, P.; Han, S.; Mani Rajan, M. S.; Choudhury, P. K.; Singh, R. Brewster mode-enhanced sensing with hyperbolic metamaterial. *Advanced Optical Materials* **2019**, *7*, 1900680.

(8) Takayama, O.; Lavrinenko, A. V. Optics with hyperbolic materials. *JOSA B* **2019**, *36*, F38–F48.

(9) Gao, W.; Doiron, C. F.; Li, X.; Kono, J.; Naik, G. V. Macroscopically Aligned Carbon Nanotubes as a Refractory Platform for Hyperbolic Thermal Emitters. *ACS Photon.* **2019**, *6*, 1602–1609.

(10) Jacob, Z.; Smolyaninov, I. I.; Narimanov, E. E. Broadband Purcell effect: Radiative decay engineering with metamaterials. *Applied Physics Letters* **2012**, *100*, 181105.

(11) Guo, Y.; Jacob, Z. Thermal hyperbolic metamaterials. *Optics express* **2013**, *21*, 15014–15019.

(12) Chang, J.-Y.; Yang, Y.; Wang, L. Tungsten nanowire based hyperbolic metamaterial emitters for near-field thermophotovoltaic applications. *International Journal of Heat and Mass Transfer* **2015**, *87*, 237–247.

(13) Elser, J.; Podolskiy, V. A.; Salakhutdinov, I.; Avrutsky, I. Nonlocal effects in effective-medium response of nanolayered metamaterials. *Applied physics letters* **2007**, *90*, 191109.

(14) Aigner, A.; Dawes, J. M.; Maier, S. A.; Ren, H. Nanophotonics shines light on hyperbolic metamaterials. *Light, Science & Applications* **2022**, *11*, 26.

(15) Guo, P.; Diroll, B. T.; Huang, W.; Zeng, L.; Wang, B.; Bedzyk, M. J.; Facchetti, A.; Marks, T. J.; Chang, R. P.; Schaller, R. D. Low-loss near-infrared hyperbolic metamaterials with epitaxial ITO-In2O3 multilayers. *Acs Photonics* **2018**, *5*, 2000–2007.

(16) Issah, I.; Pihlava, T.; Rashed, A. R.; Caglayan, H. Mechanism of emitters coupled with a polymer-based hyperbolic metamaterial. *Optics Express* **2022**, *30*, 8723–8733.

(17) Sreekanth, K. V.; Luca, A. D.; Strangi, G. Experimental demonstration of surface and bulk plasmon polaritons in hypergratings. *Scientific reports* **2013**, *3*, 1–7.

(18) Yan, R.; Wang, T.; Wang, H.; Yue, X.; Wang, L.; Wang, Y.; Zhang, J. Effective excitation of bulk plasmon-polaritons in hyperbolic metamaterials for high-sensitivity refractive index sensing. *Journal of Materials Chemistry C* **2022**, *10*, 5200–5209.

(19) Liu, R.; Zha, Z.; Shafi, M.; Li, C.; Yang, W.; Xu, S.; Liu, M.; Jiang, S. Bulk plasmon polariton in hyperbolic metamaterials excited by multilayer nanoparticles for surface-enhanced Raman scattering (SERS) sensing. *Nanophotonics* **2021**, *10*, 2949–2958.

(20) Sreekanth, K. V.; ElKabbash, M.; Alapan, Y.; Rashed, A. R.; Gurkan, U. A.; Strangi, G. A multiband perfect absorber based on hyperbolic metamaterials. *Scientific reports* **2016**, *6*, 1–8.

(21) Lee, Y. U.; Nie, Z.; Li, S.; Lambert, C.-H.; Zhao, J.; Yang, F.; Wisna, G. B. M.; Yang, S.; Zhang, X.; Liu, Z. Ultrathin Layered Hyperbolic Metamaterial-Assisted Illumination Nanoscopy. *Nano Letters* **2022**, *22*, 5916–5921.

(22) Caldwell, J. D.; Kretinin, A. V.; Chen, Y.; Giannini, V.; Fogler, M. M.; Francescato, Y.; Ellis, C. T.; Tischler, J. G.; Woods, C. R.; Giles, A. J., et al. Sub-diffractional volume-confined polaritons in the natural hyperbolic material hexagonal boron nitride. *Nature communications* **2014**, *5*, 1–9.

(23) Li, P.; Dolado, I.; Alfaro-Mozaz, F. J.; Casanova, F.; Hueso, L. E.; Liu, S.; Edgar, J. H.; Nikitin, A. Y.; Vélez, S.; Hillenbrand, R. Infrared hyperbolic metasurface based on nanostructured van der Waals materials. *Science* **2018**, *359*, 892–896.

(24) Matveeva, O.; Tresguerres-Mata, A.; Kirtaev, R.; Voronin, K.; Taboada-Gutiérrez, J.; Lanza, C.; Duan, J.; Martín-Sánchez, J.; Volkov, V.; Alonso-González, P., et al. Twist-tunable polaritonic nanoresonators in a van der Waals crystal. *npj 2D Materials and Applications* **2023**, *7*, 31.

(25) Huang, W.; Folland, T. G.; Sun, F.; Zheng, Z.; Xu, N.; Xing, Q.; Jiang, J.; Chen, H.;

Caldwell, J. D.; Yan, H., et al. In-plane hyperbolic polariton tuners in terahertz and long-wave infrared regimes. *Nature Communications* **2023**, *14*, 2716.

(26) Roberts, J. A.; Yu, S.-J.; Ho, P.-H.; Schoeche, S.; Falk, A. L.; Fan, J. A. Tunable hyperbolic metamaterials based on self-assembled carbon nanotubes. *Nano Letters* **2019**, *19*, 3131–3137.

(27) Schöche, S.; Ho, P.-H.; Roberts, J. A.; Yu, S. J.; Fan, J. A.; Falk, A. L. Mid-IR and UV-Vis-NIR Mueller Matrix Ellipsometry Characterization of Tunable Hyperbolic Metamaterials Based on Self-Assembled Carbon Nanotubes. *J. Vac. Sci. Technol. B* **2020**, *38*, 014015.

(28) Headrick, R. J.; Tsentalovich, D. E.; Berdegué, J.; Bengio, E. A.; Liberman, L.; Kleinerman, O.; Lucas, M. S.; Talmon, Y.; Pasquali, M. Structure–property relations in carbon nanotube fibers by downscaling solution processing. *Advanced Materials* **2018**, *30*, 1704482.

(29) Roberts, J. A.; Ho, P.-H.; Yu, S.-J.; Wu, X.; Luo, Y.; Wilson, W. L.; Falk, A. L.; Fan, J. A. Multiple tunable hyperbolic resonances in broadband infrared carbon-nanotube metamaterials. *Physical Review Applied* **2020**, *14*, 044006.

(30) Maradudin, A.; Simonsen, I.; Polanco, J.; Fitzgerald, R. Rayleigh and Wood anomalies in the diffraction of light from a perfectly conducting reflection grating. *Journal of Optics* **2016**, *18*, 024004.

(31) Komatsu, N.; Ichinose, Y.; Dewey, O. S.; Taylor, L. W.; Trafford, M. A.; Yomogida, Y.; Wehmeyer, G.; Pasquali, M.; Yanagi, K.; Kono, J. Macroscopic weavable fibers of carbon nanotubes with giant thermoelectric power factor. *Nature Communications* **2021**, *12*, 4931.

(32) Ma, W.; Alonso-González, P.; Li, S.; Nikitin, A. Y.; Yuan, J.; Martín-Sánchez, J.;

Taboada-Gutiérrez, J.; Amenabar, I.; Li, P.; Vélez, S., et al. In-plane anisotropic and ultra-low-loss polaritons in a natural van der Waals crystal. *Nature* **2018**, *562*, 557–562.

(33) Passler, N. C.; Ni, X.; Hu, G.; Matson, J. R.; Carini, G.; Wolf, M.; Schubert, M.; Alù, A.; Caldwell, J. D.; Folland, T. G., et al. Hyperbolic shear polaritons in low-symmetry crystals. *Nature* **2022**, *602*, 595–600.

(34) Dai, S.; Fei, Z.; Ma, Q.; Rodin, A.; Wagner, M.; McLeod, A.; Liu, M.; Gannett, W.; Regan, W.; Watanabe, K., et al. Tunable phonon polaritons in atomically thin van der Waals crystals of boron nitride. *Science* **2014**, *343*, 1125–1129.

(35) Jinkins, K. R.; Chan, J.; Jacobberger, R. M.; Berson, A.; Arnold, M. S. Substrate-Wide Confined Shear Alignment of Carbon Nanotubes for Thin Film Transistors. *Advanced Electronic Materials* **2019**, *5*, 1800593.

(36) Vasilantonakis, N.; Nasir, M. E.; Dickson, W.; Wurtz, G. A.; Zayats, A. V. Bulk plasmon-polaritons in hyperbolic nanorod metamaterial waveguides. *Laser & photonics reviews* **2015**, *9*, 345–353.

(37) Maier, S. *Plasmonics - Fundamentals and Applications*; Springer, 2007.

(38) Hutley, M. C. *Diffraction gratings*; Academic Press, 1990.

(39) Low, T.; Chaves, A.; Caldwell, J. D.; Kumar, A.; Fang, N. X.; Avouris, P.; Heinz, T. F.; Guinea, F.; Martin-Moreno, L.; Koppens, F. Polaritons in layered two-dimensional materials. *Nature materials* **2017**, *16*, 182–194.

(40) Jacob, Z. Hyperbolic phonon–polaritons. *Nature materials* **2014**, *13*, 1081–1083.

(41) Lyashko, E. I.; Maimistov, A. I. Guided waves in asymmetric hyperbolic slab waveguides: the TM mode case. *JOSA B* **2016**, *33*, 2320–2330.

(42) Wang, P.; Krasavin, A. V.; Liu, L.; Jiang, Y.; Li, Z.; Guo, X.; Tong, L.; Zayats, A. V. Molecular Plasmonics with Metamaterials. *Chemical Reviews* **2022**, *122*, 15031–15081.

(43) Wang, P.; Nasir, M. E.; Krasavin, A. V.; Dickson, W.; Jiang, Y.; Zayats, A. V. Plasmonic metamaterials for nanochemistry and sensing. *Accounts of chemical research* **2019**, *52*, 3018–3028.

(44) Li, W.; Valentine, J. Metamaterial perfect absorber based hot electron photodetection. *Nano letters* **2014**, *14*, 3510–3514.

(45) Babar, S.; Weaver, J. H. Optical constants of Cu, Ag, and Au revisited. *Appl. Opt.* **2015**, *54*, 477–481.

(46) Chandler-Horowitz, D.; Amirtharaj, P. M. High-accuracy, midinfrared (450 cm- 1 $\leq$ $\omega \leq$ 4000 cm^{-1}) refractive index values of silicon. *Journal of Applied physics* **2005**, *97*, 123526.

TOC Graphic

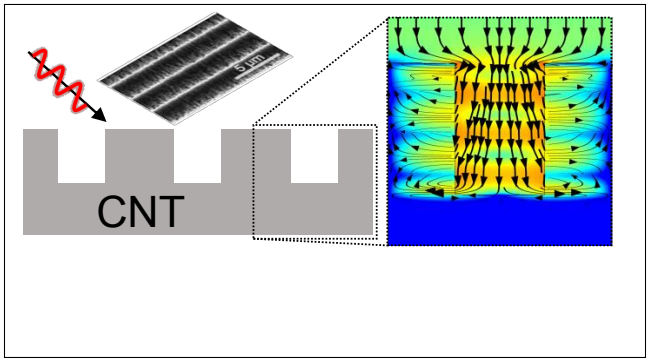

Supporting Information for: Coupling into Hyperbolic Carbon-Nanotube Films with a Deep-Etched Antenna Grating

Bryant B. Jerome,[1,2,†] Ciril S. Prasad,[1,2,†] Andrea Schirato,[1,3,4,†] Oliver S. Dewey,[5,6,7,8,9] Jacques Doumani,[1,2] Andrey Baydin,[1,8] Weilu Gao,[10,9] Giuseppe Della Valle,[3,11] Junichiro Kono,[1,7,8,12] Matteo Pasquali,[5,6,7,8,9] Gururaj Naik,[*,1] and Alessandro Alabastri[*,1]

[1] *Department of Electrical and Computer Engineering, Rice University, Houston, Texas 77005, USA*

[2] *Applied Physics Graduate Program, Smalley-Curl Institute, Rice University, Houston, Texas, 77005, USA*

[3] *Department of Physics, Politecnico di Milano, Piazza Leonardo da Vinci, 32, 20133 Milano, Italy*

[4] *Istituto Italiano di Tecnologia, via Morego 30, 16163, Genoa, Italy*

[5] *Department of Chemical and Biomolecular Engineering, Rice University, Houston, Texas 77005, USA*

[6] *Department of Chemistry, Rice University, Houston, Texas, 77005, USA*

[7] *Department of Material Science and NanoEngineering, Rice University, Houston, Texas 77005, USA*

[8] *Smalley-Curl Institute, Rice University, Houston, Texas, 77005, USA*

[9] *The Carbon Hub, Rice University, Houston, Texas, 77005, USA*

[10] *Department of Electrical and Computer Engineering, The University of Utah, Salt Lake City, UT, USA*

[11] *Istituto di Fotonica e Nanotecnologie - Consiglio Nazionale delle Ricerche, Piazza Leonardo da Vinci, 32, I-20133 Milano, Italy*

[12] *Department of Physics and Astronomy, Rice University, Houston, Texas 77005, USA*

[†] *Contributed equally to this work*

S1: Dispersion Relation Derivation

Maxwell's equations state an electric field applied to a material, $\mathbf{E}$, is constrained such that:[1]

$$\mathbf{k} \times (\mathbf{k} \times \mathbf{E}) + \omega^2 \mu_0 \bar{\varepsilon} \mathbf{E} = 0 \tag{S1}$$

$$\begin{bmatrix} k_0^2 \varepsilon_{xx} - k_y^2 - k_z^2 & k_x k_y & k_x k_z \\ k_x k_y & k_0^2 \varepsilon_{yy} - k_x^2 - k_z^2 & k_y k_z \\ k_x k_z & k_y k_z & k_0^2 \varepsilon_{zz} - k_x^2 - k_y^2 \end{bmatrix} \begin{bmatrix} E_x \\ E_y \\ E_z \end{bmatrix} = 0 \tag{S2}$$

The eigenvalue equations reduces the solution to:

$$k_0^4 = k_0^2 \left[k_x^2 \left(\frac{1}{\varepsilon_{yy}} + \frac{1}{\varepsilon_{zz}} \right) + k_y^2 \left(\frac{1}{\varepsilon_{xx}} + \frac{1}{\varepsilon_{zz}} \right) + k_x^2 \left(\frac{1}{\varepsilon_{xx}} + \frac{1}{\varepsilon_{yy}} \right) \right] - k^2 \left(\frac{k_x^2}{\varepsilon_{yy}\varepsilon_{zz}} + \frac{k_y^2}{\varepsilon_{xx}\varepsilon_{zz}} + \frac{k_z^2}{\varepsilon_{xx}\varepsilon_{yy}} \right) \tag{S3}$$

where $k^2 = k_x^2 + k_y^2 + k_z^2$. This is the full dispersion relation for any material, with two solutions dedicated to TM modes, and two solutions to TE modes.

Assuming the material is uniaxial (i.e., $\varepsilon_{yy} = \varepsilon_{zz}$) simplifies the above equation into:

$$\left(k^2 - \varepsilon_{zz} k_0^2 \right) \left(\frac{k_x^2}{\varepsilon_{zz}} + \frac{k_y^2 + k_z^2}{\varepsilon_{xx}} - k_0^2 \right) = 0 \tag{S4}$$

from which Eq. 1 in the main text is taken.

By then combining this analytical expression for the dispersion of bulk hyperbolic modes with the experimental estimation of the hyperbolic medium permittivity tensor ($\varepsilon_{xx}, \varepsilon_{yy}, \varepsilon_{zz}$), one could determine the couples of (k_x, k_z) momentum components (assuming, again, $k_y = 0$, as in our experimental conditions) associated with such modes.

In particular, Fig. S1 shows some cuts of the isofrequency surfaces defined by the wave-vectors fulfilling the dispersion relation (Eq. 1 from the main text) holding within our CNT film, based on the permittivity component we measured (Fig. 2d in the main text). The resulting contours of in-plane (k_x) against out-of-plane (k_z) wave-vector components allowed

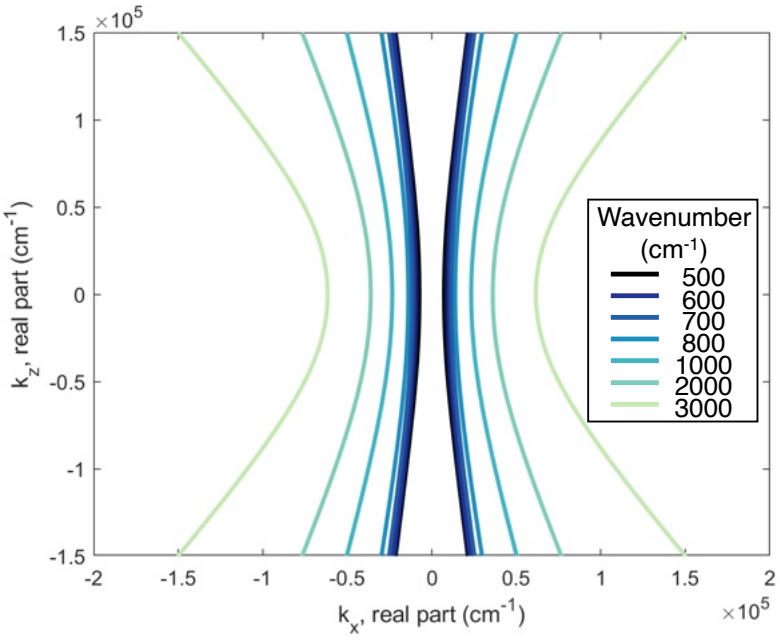

Figure S1: Isofrequency contours obtained for the momentum z and x components (real parts) fulfilling Equation 1 of the main text by considering the measured permittivity tensor of our CNT film.

within the CNT film show the typical hyperbolic branches characterizing anisotropic systems. This indicates that the bulk modes sustained within the CNT film, given the experimental permittivity tensor components, have a hyperbolic character.

Generally, in order to directly couple light from free space into a hyperbolic system, a diffraction grating can be employed, to overcome a phase mismatch. Indeed, from Maxwell's equations (more specifically, Gauss's law), it can be shown that, across an interface separating two uncharged media, one has $k_{||,1} = k_{||,2}$, where $k_{||,1}$ indicates the wavenumber of light in medium 1 moving parallel to the interface, and $k_{||,2}$ indicates the same for medium 2. For an incidence light source travelling in an isotropic medium 1, $k_{||} = n_1 k_0 \sin\theta$, where n_1 is the refractive index of medium 1, θ is the angle of incidence, $k_0 = \frac{\omega}{c}$, ω is the angular frequency of the light, and c is the speed of light in vacuum. From Eq. 1 in main text, for an extraordinary wave excited from free space to couple into a uniaxial medium (assuming

the interface lies in x, with $\varepsilon_{zz} > 0, \varepsilon_{xx} < 0$), the phase matching condition reads:[2]

$$k_0 \sin\theta = k_x = \sqrt{\varepsilon_{yy,zz}\left(k_0^2 - \frac{k_z^2}{\varepsilon_{xx}}\right)} = \varepsilon_{yy,zz}^{1/2} k_0 \sqrt{1 + \frac{k_z^2}{k_0^2}\left|\frac{1}{\varepsilon_{xx}}\right|}. \tag{S5}$$

Assuming $\varepsilon_{xx} < 0$ and $\varepsilon_{yy,zz} > 1$, it is impossible to directly fulfill this phase matching condition. Conventionally in these cases, coupling is enabled by either increasing the refractive index of the source medium, or by providing additional k_x momentum via constructive interference from a diffraction grating. With an additional momentum contributions from the grating, k_x becomes:[3]

$$k_x = k_0\left(\sin\theta + \frac{n\lambda}{a}\right) = k_0 \sin\theta + n\frac{2\pi}{a} \tag{S6}$$

where a is the periodicity of the diffraction grating, and n is an integer numbering the diffraction order. From Eq. S5 and Eq. S6, we estimate the maximum value of k_0 that can couple into the hyperbolic anisotropic medium from free space is given by:

$$k_0 = \frac{n\frac{2\pi}{a}}{\sqrt{\varepsilon_{yy,zz}} - \sin\theta} = k_{x,\mathrm{film}}^n. \tag{S7}$$

S2 : Dielectric constants of ITO+In_2O_3

For a HM consisting of alternating metals/dielectrics stacked on top of each other, the effective dielectric constants derived from the Effective Medium Approximation (EMA) are:[4]

$$\varepsilon_{xx}^{\mathrm{bulk}} = F\varepsilon_{\mathrm{metal}} + (1-F)\varepsilon_{\mathrm{dielectric}}$$

$$\varepsilon_{zz}^{\mathrm{bulk}} = \frac{1}{\frac{1}{F\varepsilon_{\mathrm{metal}}} + \frac{1}{(1-F)\varepsilon_{\mathrm{dielectric}}}} \tag{S8}$$

where F is the thickness of the metal divided by the thickness of the metal+dielectric bilayer, $\varepsilon_{\mathrm{metal}}$ is the isotropic dielectric constant of the metal, and $\varepsilon_{\mathrm{dielectric}}$ is the isotropic dielectric

constant of the dielectric. Using this formula, we calculate the effective dielectric constants of the ITO+In_2O_3 HM discussed in Fig. 1 of the main text . The effective dielectric constants, along with the isotropic constants of ITO and In_2O_3 extracted from a Drude fit provided by ref.,[5] is presented in Fig. S2 .

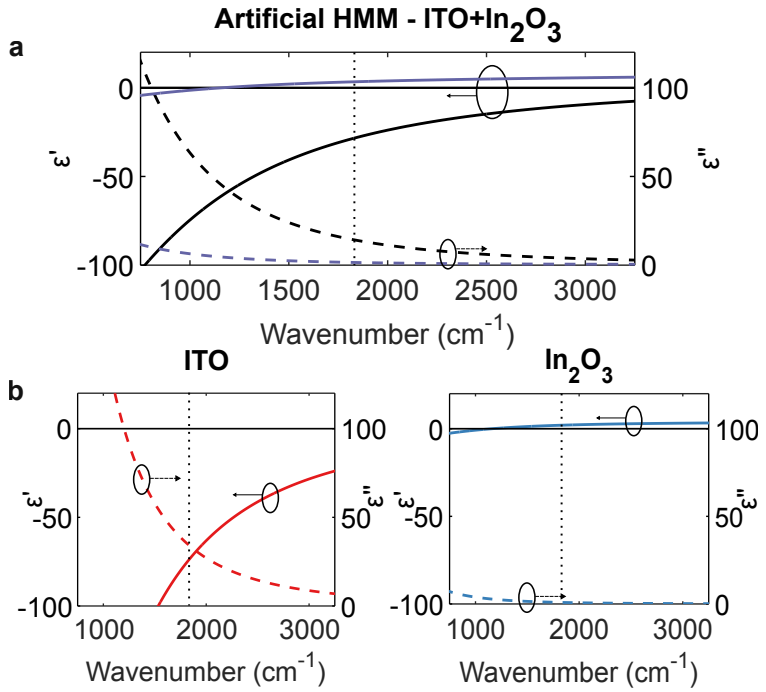

Figure S2: a) Effective dielectric constants of an ITO+In_2O_3 multilayer HMM, where the thickness of the In_2O_3 layer is fixed at 1.5 times the thickness of the ITO layer. b) Dielectric constants of isotropic ITO and In_2O_3. The wavenumber analyzed in Fig. 1 is marked by the dotted line.

The mulitlayer ITO+In_2O_3 HMM has $\varepsilon_{xx} = -28.42 + 14.28i$ and $\varepsilon_{zz} = 3.37 + 1.53i$ at $1830\,\mathrm{cm}^{-1}$, and $k_x = k_0 \sin(0°) + n\frac{2\pi}{2\,\mu\mathrm{m}}$ (see Eq. S6). Thus, for first order grating coupling, neglecting the imaginary part of ε_{xx} and ε_{yy}, the dispersion relation of Eq. 1 gives:

$$\frac{\pi^2}{3.37}\mu\mathrm{m}^{-2} + \frac{k_z^2}{-28.42} = \left(2\pi \cdot 0.19\,\mu\mathrm{m}^{-1}\right)^2$$

$$\frac{k_z^2}{-28.42} = \left(1.43 - \frac{\pi^2}{3.37}\right)\mu\mathrm{m}^{-2} = -1.50\,\mu\mathrm{m}^{-2}$$

$$k_z = \left(\sqrt{42.7\,\mu\mathrm{m}^{-2}}\right) = 6.54\,\mu\mathrm{m}^{-1} \quad \text{(S9)}$$

This k_z does not meaningfully contribute to the electric field plots of Fig. 1 , pointing towards bulk plasmon polaritons dominating the coupling within the multilayer heterostructure.

S3: Optical anisotropy in aligned CNT films

Strong optical anisotropy of our aligned CNT film is evident from the measured permittivities reported in Fig. 2d of the main text. The in-plane anisotropy in x, y directions arise due to the alignment of CNTs along x axis that renders it metallic along that direction (x-axis) and dielectric along perpendicular direction (y-axis). To further elucidate this anisotropy, we performed polarized reflection measurements on as-prepared CNT films and CNT grating described in Fig. 3 of the main text. As expected from the above mentioned in-plane anisotropy, both the as-prepared CNT film and CNT grating showed distinct reflection spectra for x and y polarized incident radiation. Since the grating periodicity is along the x-axis, hyperbolic coupling occur only for the x-polarized radiation and the response for y-polarized light remain similar for both as-prepared CNT film and after etching grating on to the film. Further, due to the optical anisotropy reported in the $y - z$ plane, the measured reflection spectra for y and $y - z$ polarized radiation are distinct for a fixed angle of incidence (see Fig. S3c).

S4: Effect of annealing on CNT optical constants

The significant red shift in the plasma frequency along x-direction caused by high temperature annealing was discussed in Fig. 2d of the main text. This is attributed to the high-temperature induced de-doping due to the removal of acidic residue from the fabrication process. Since this de-doping is independent of direction, the process of annealing inflict similar effects on the optical properties along other directions as shown in Fig. S4. We used as-prepared CNT films for fabricating the CNT grating as they give a larger hyperbolic bandwidth.

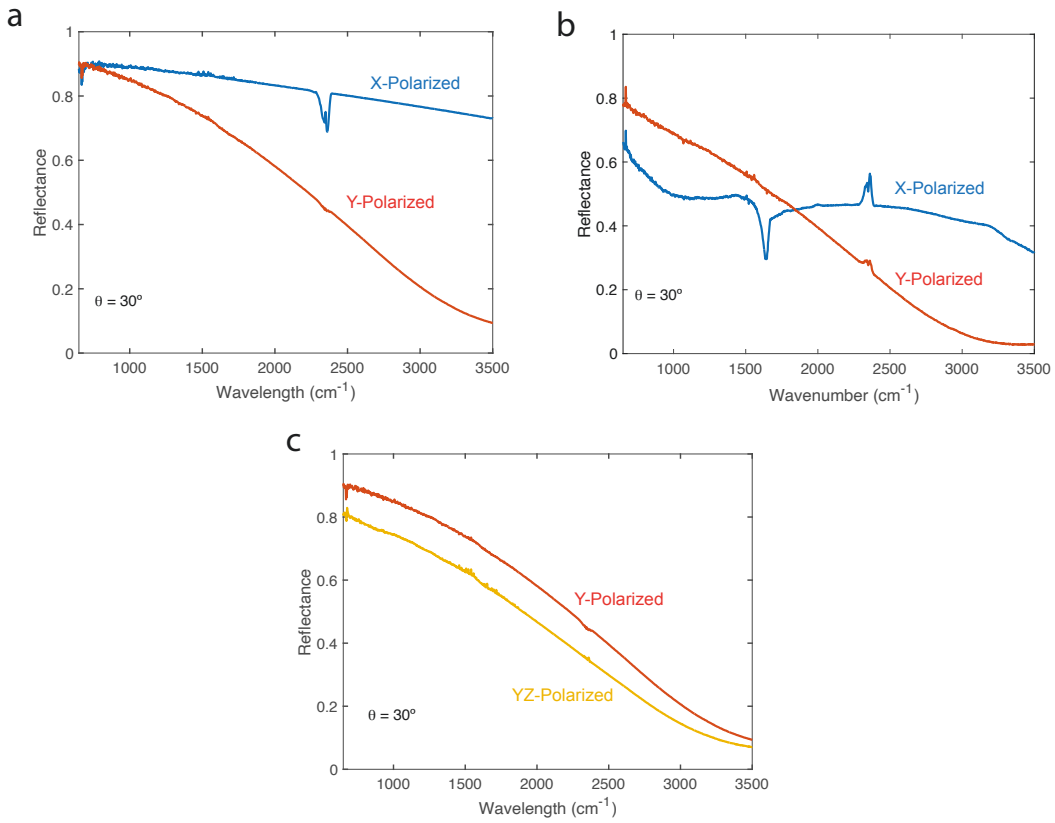

Figure S3: a) Measured reflection spectra for as-prepared CNT film (before etching) for x and y polarized incident radiation at an angle of incidence 30°, b) Measured reflection spectra after etching gratings on the same film for x and y polarized incident radiation at an angle of incidence 30°, c) The measured reflection spectra for y-polarized and yz-polarized incident radiation at an angle of incidence 30°.

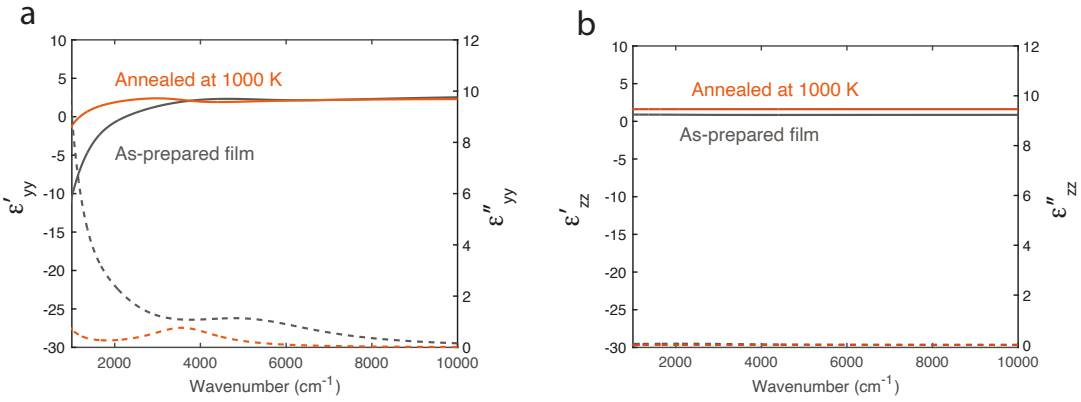

Figure S4: a) Y-axis and b) Z-axis dielectric constants of as-prepared and annealed (at 1000 K) aligned CNT films, displaying de-doping effects.

S5: Surface plasmon polaritons (SPP)

The SPP for a material illuminated from free space (angle of incidence θ, incident wave-vector k_0) can be resonantly excited with wave-vector in-plane component:[6]

$$k_x = k_0 \sin\theta = k_0 \sqrt{\frac{\varepsilon_{xx}}{1+\varepsilon_{xx}}} \tag{S10}$$

A diffraction grating contributes with an additional $n\frac{2\pi}{a}$ momentum (a being the grating period) in k_x, allowing SPP excitations to occur when θ is small. Note that, for our shear-aligned CNT film with $a = 4\,\mu\text{m}$ diffraction grating and $\theta = 0$, the SPP resonance occurs at approximately 2500 cm^{-1}.

Evidently, the grating period (a) is crucial in determining the phase matching condition for SPP excitation. To sample the dispersion of the main SPP observed in our CNT film, we performed measurements for a fixed angle of incidence (30°) on structures featuring different grating periods. Figure S5a compares the reflectance spectra of the sample detailed in the main text (a =4 µm, p =2 µm) and another sample with a = 6 µm and p =3 µm, keeping other parameters and illumination conditions unchanged. Different grating periods allow for exciting different modes, as the coupling conditions get altered. In particular, the SPP mode experiences a red-shift, moving from $\sim$ 1600 to $\sim$ 1100 cm^{-1}. These SPP excitations are launched thanks to an additional momentum coming from the -1 diffraction order of the grating (see the dispersion relations in Fig. S5b). In fact, for larger periodicity, an additional dip arises at $\sim$ 3000 cm^{-1}, corresponding to the frequency at which the SPP dispersion relation intersects the tilted light line with the additional contribution $+2\pi/a$, as illustrated indeed in Fig. S5b.

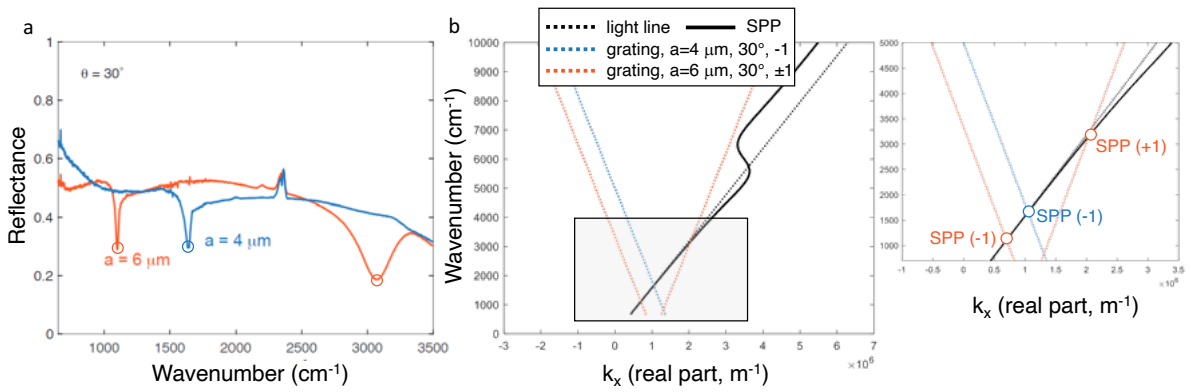

Figure S5: a) Measured reflectance spectra for $a = 4\,\mu\text{m}$ (blue curve) and $a = 6\,\mu\text{m}$ (red curve) CNT grating in the same experimental conditions as in Fig. 3b of the main text. b) Dispersion relation of the SPP according to Eq. (S10) (black), plotted alongside the tilted light lines with corresponding grating contributions. Lines intersections give the spectral position of the SPP resonances across the measures spectra.

Note that for our peculiar system, where also the antennas making up the grating contribute themselves to excite modes, the groove thickness is also a relevant parameter of the structure configuration. This is true both in terms of coupling the incident light (see Section S6 for more details) and outcoupling radiation. To gain more information about the outcoupling process from the etched film, we simulated and inspected the electric field pattern across structures with the same grating period, but different antenna grooves.

Small thicknesses are expected to be mostly associated with surface excitations such as SPPs, while thicker wedges will have more contributions from modes localised within the antenna volumes (as it is for Fabry-Pérot (FP) resonances). Figure S6 compares the electromagnetic response of the systems analysed in Fig. 4 of the main text with the smallest ($0.4\,\mu\text{m}$) and largest ($10\,\mu\text{m}$) grating thickness for a frequency close to the SPP-matching condition ($2500\ \text{cm}^{-1}$) and another close to a resonant dip in reflectance for the thick-grating system ($2150\ \text{cm}^{-1}$) as reported in Fig. 6a. The numerical analysis of the two systems suggest that indeed close to the SPP resonant excitation condition, the electric field is mostly localized at the grating surface for both the simulated thickness values. At $2150\ \text{cm}^{-1}$ instead, the thick grating supports a modal pattern with high enhancement well-localized within the antennas forming the grating. This produces the dip in reflection

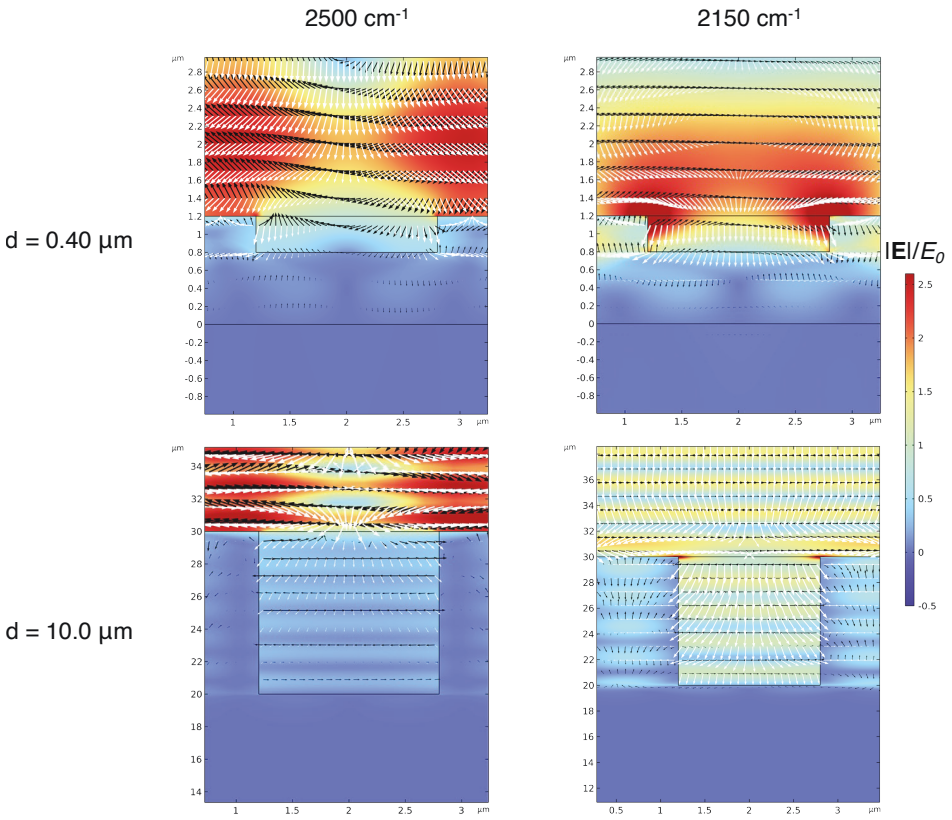

Figure S6: The electromagnetic response of the systems analysed in Figure 4 of the main text with 0.4 µm (top panels) and 10 µm (bottom panels) grating thickness at frequencies 2500 cm^{-1} (left panels) and 2150 cm^{-1} (right panels). Black arrows represent the electric field vector field, white arrows are the Poynting vector field, while colours refer to the electric field enhancement.

observed at the considered frequency, thanks to such an extra absorptive channel introduced by the antennas of the grating. On the contrary, the thin grating, despite a larger penetration in the material compared to the same structure at 2500 cm^{-1}, does not show any specific localized pattern across the grating, which as such does not couple efficiently via FP antenna modes to radiation.

S6: Confined hyperbolic plasmon modes in CNT Fabry-Pérot nanoresonators upon variations of the experimental geometry

By inspecting the measured reflectance of the sample and with the aid of numerical simulations, we here investigate the presence of optical response of confined hyperbolic polariton modes (HPMs) supported by the Fabry-Pérot (FP) nanoantennas composing the etched grating. Due to the sample characteristics and experimental conditions, such modes are weakly excited across the measured reflectance (Fig. 3 in the main text) and appear as shallow dips. In particular, the experimental feature we relate to confined HPM excitation is the dip at around 1000 cm^{-1} observed in the measured spectra (Fig. 3c in the main text), that indeed our experimental conditions make particularly broad and hard to identify precisely. However, by tweaking the sample geometrical parameters and identifying the most critical ones, simulations make FP cavity-confined HPM excitation clearer, highlighting in particular the role played by thicker grating grooves. This is done in the numerical analysis reported in the main text (Fig. 4), where geometrical modifications of the structure are aimed at promoting the excitation of the HPMs, increasing their contribution over the spectrum. Here, to ascertain more thoroughly that our mode analysis is pertinent and consistent, and the spectral feature we focused on is indeed related to a strongly confined mode within the antennas composing the etched grating, we have complemented the calculations reported in the main text with a detailed study of the evolution of the mode associated with the experimental dip upon the changes in parameters considered.

In the following, we report a series of figures showing how electric field enhancement spatial distribution maps and both (normalized) electric and Poynting vector fields evaluated at this mode (identified as empty dot in the top left panel) evolve for each parameter value. The same analysis is repeated for each curve of Fig. 4. This enables us to follow the same mode in each of the cases considered, i.e. after changing the incidence angle (Fig. 4a and

Fig. S7), the grating slope (Fig. 4b and Fig. S8), the grating thickness (Fig. 4c and Fig. S9) and the CNT losses (Fig. 4d and Fig. S10), by verifying that the dispersive mode under scrutiny is associated with the same modal pattern in each structure after a slight parametric change. For the sequence of modes reported below, the bottom right mode of a figure corresponds to the top left mode of the following one.

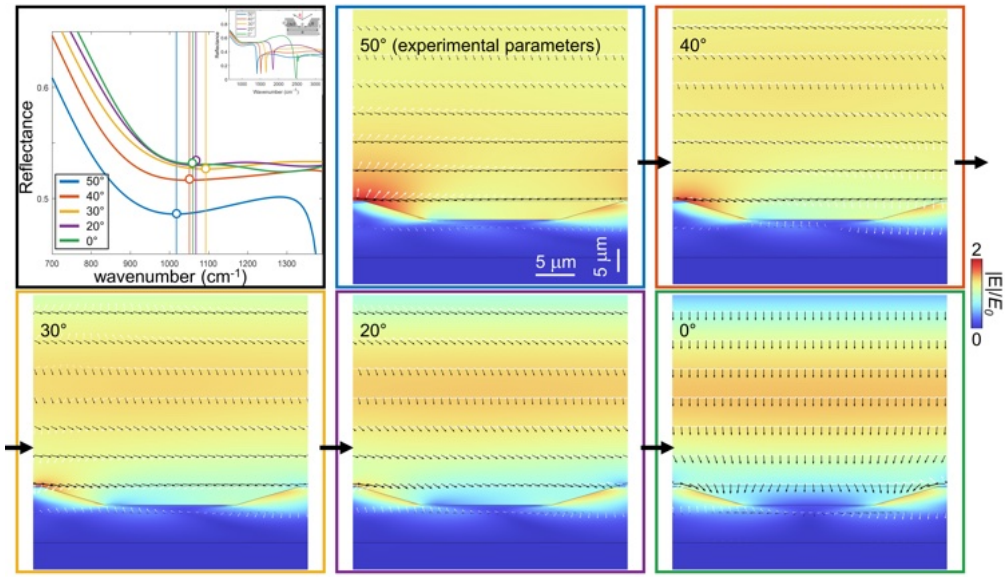

Figure S7: Reducing angle of incidence. Top left: zoom-in of the calculated reflectance spectra shown in Fig. 4a, as a function of the incident angle, from the experimental values (50°, 40°, 30°) to 20°, 0°. Empty dots highlight the dip associated with the confined hyperbolic mode in each curve. From middle top to bottom right: the electric field enhancement spatial distribution evaluated at the corresponding confined HPM frequency (empty dots in the spectra) is shown for each structure after the corresponding geometrical change. White arrows display the electric vector field, black arrows represent the Poynting vector.

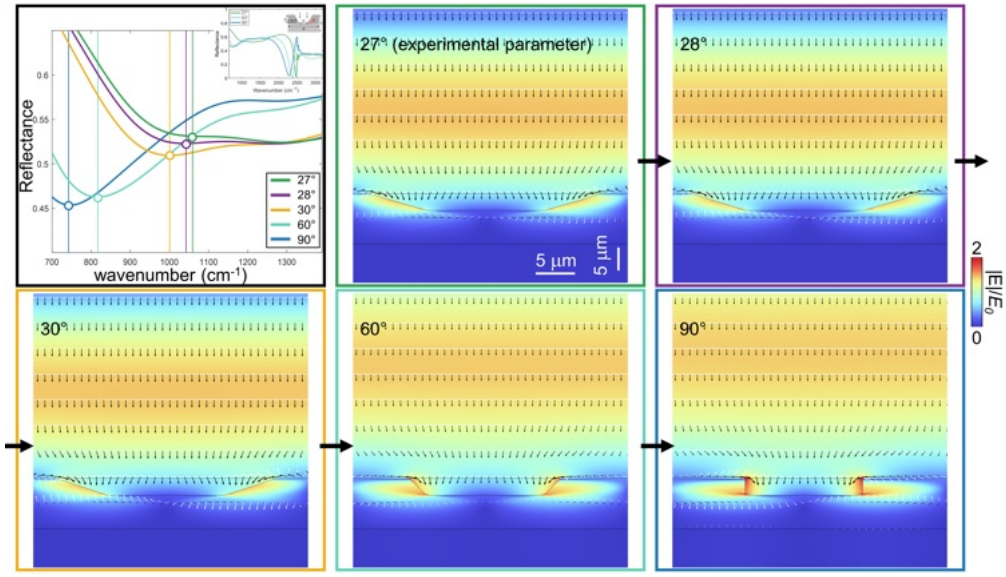

Figure S8: Increasing grating slide. Top left: zoom-in of the calculated reflectance spectra shown in Fig. 4b, as a function of the grating slope, from the experimental values (27°) to 28°, 30°, 60°, 90°. Empty dots highlight the dip associated with the confined hyperbolic mode in each curve. From middle top to bottom right: the electric field enhancement spatial distribution evaluated at the corresponding confined HPM frequency (empty dots in the spectra) is shown for each structure after the corresponding geometrical change. White arrows display the electric vector field, black arrows represent the Poynting vector.

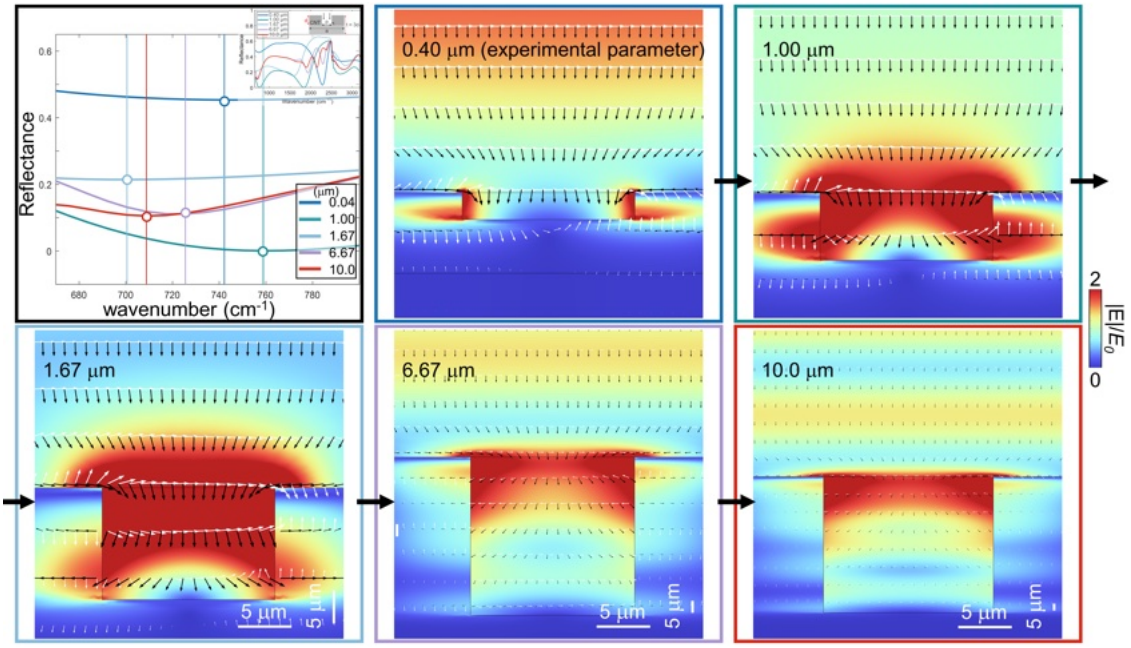

Figure S9: Increasing grating thickness. Top left: zoom-in of the calculated reflectance spectra shown in Fig. 4c, as a function of the grating thickness, from the experimental values (0.4 µm) to 1 µm, 1.67 µm, 6.67 µm, 10 µm. Empty dots highlight the dip associated with the confined hyperbolic mode in each curve. From middle top to bottom right: the electric field enhancement spatial distribution evaluated at the corresponding confined HPM frequency (empty dots in the spectra) is shown for each structure after the corresponding geometrical change. White arrows display the electric vector field, black arrows represent the Poynting vector.

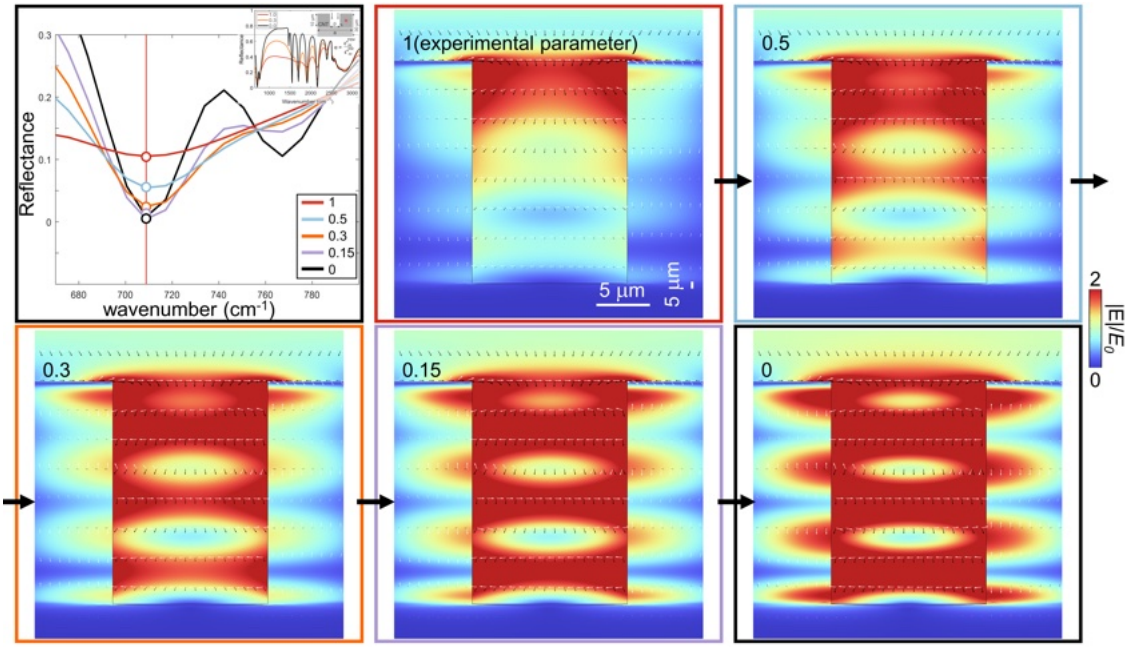

Figure S10: Reducing CNT losses. Top left: zoom-in of the calculated reflectance spectra shown in Fig. 4b, as a function of the CNT permittivity losses, from the experimental values (1) to 0.5, 0.3, 0.15, 0. Empty dots highlight the dip associated with the confined hyperbolic mode in each curve. From middle top to bottom right: the electric field enhancement spatial distribution evaluated at the corresponding confined HPM frequency (empty dots in the spectra) is shown for each structure after the corresponding geometrical change. White arrows display the electric vector field, black arrows represent the Poynting vector.

This analysis, showing that the frequency investigated produces exactly the same modal pattern across the structure, corroborates our interpretation of the weak experimental feature observed at around 1000 cm^{-1} in the measured spectra as a dispersive confined HPM.

Moreover, to demonstrate that FP-mediated HPM excitation substantially benefits from thicker gratings, we assessed the absorptance of the dip at this mode for each structure simulated in Fig. 4. Fig. S11 shows the obtained quantity for all cases, and highlights a dramatic increase in absorptance as a result of the grating thickness increase, and especially by going from 0.4 µm to 1.0 µm.

Indeed, by computing the spectra for intermediate thicknesses, the confined HPM under investigation (now moved to around 740 cm^{-1}) exhibits a substantial decrease in reflectance by increasing the grating thickness (Fig. S12). Additional spectra, obtained by further

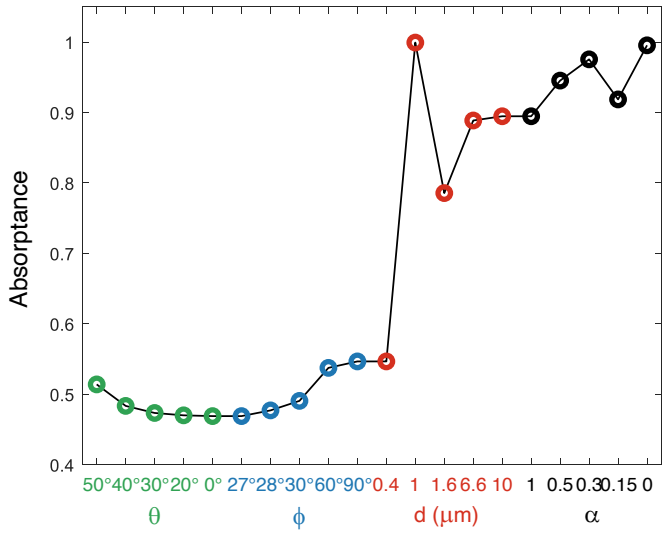

Figure S11: Absorptance of the confined hyperbolic plasmon mode identified in Fig. S7-S10 by empty dots for each of the geometrical structures considered above

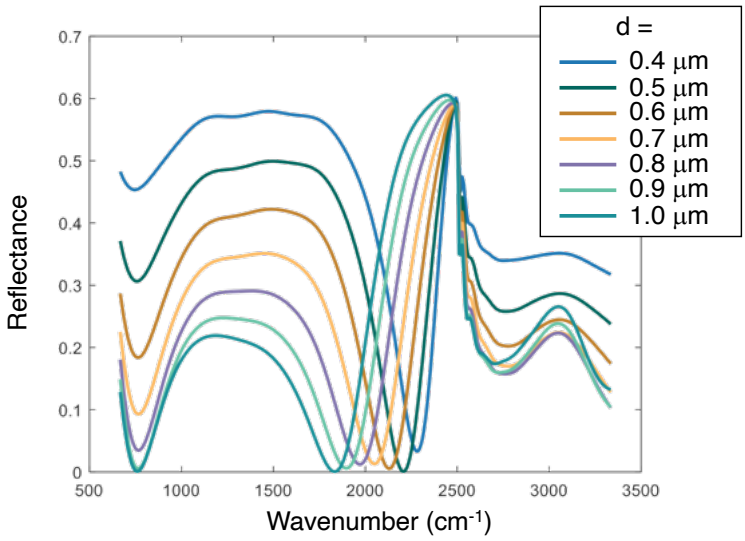

Figure S12: Calculated reflectance of the system at normal incidence and 90° grating slope by gradually varying grating thickness, from experimental (0.4 µm) to 1.0 µm. The confined HPM mode sits at 742 cm^{-1} and experiences a substantial decrease in reflectance amplitude (absorptance increase) by increasing the thickness.

increasing the thickness of the grooves, are also reported in Fig. S13

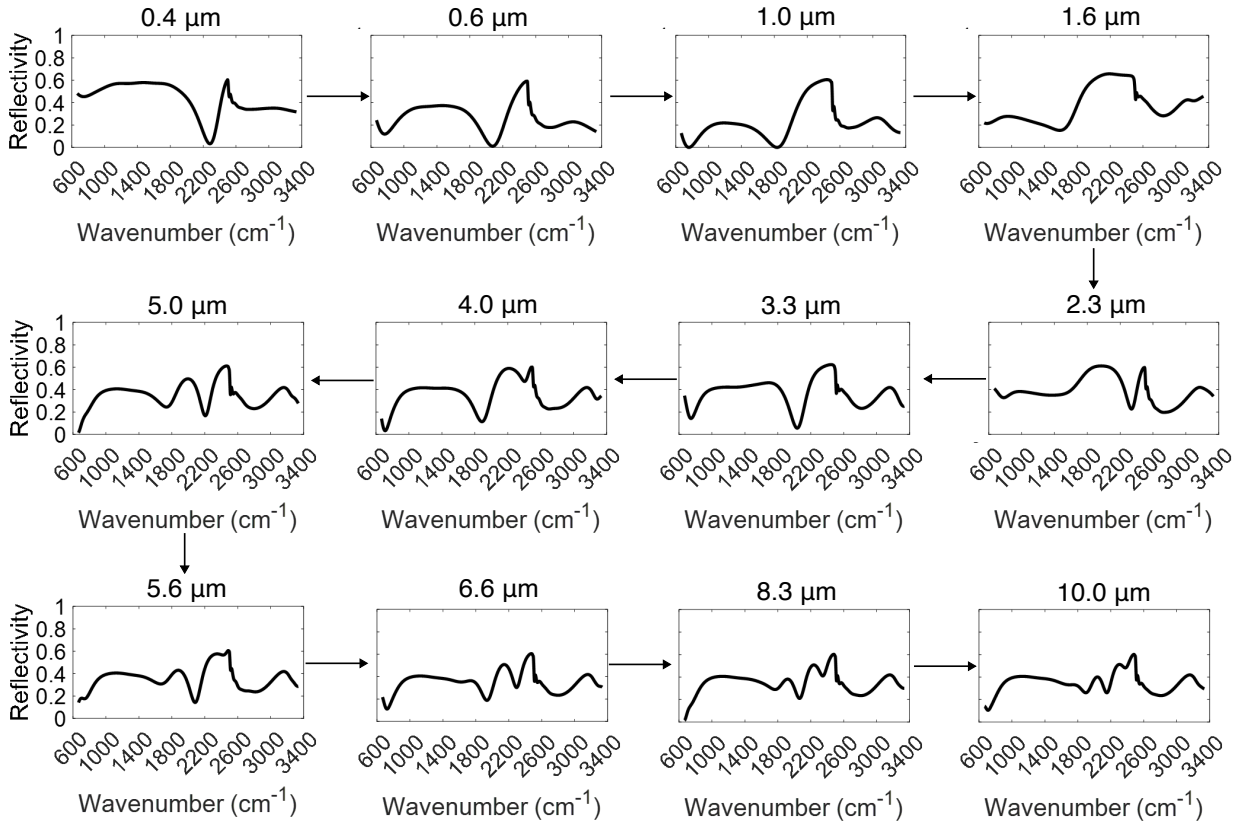

Figure S13: FEM reflection for the aligned CNT film, with varying thickness d from 0.4 µm to 10 µm

This observation is taken as a compelling demonstration of the role of the antennas composing the grating, and it reinforces the idea that a larger contribution from the cavity/antenna fosters the efficient confinement of HPMs, providing an explanation for the fact that, in our sample, such modes are weakly excited (thin grating).

The system's optical response is also affected by variations in the grating periodicity. In particular, smaller periods (deep subwavelength grating regime) lead to much stronger electromagnetic confinement effects. Fig. S14 illustrates the changes in the simulated reflectance of our structure when the grating period (a) is reduced, and the void groove width, p, is modified accordingly to keep the ratio p/a fixed. By following the confined HPM analyses, the dip observed in the experimental conditions (a=4 µm) blue shifts and broadens substantially when decreasing the periodicity. Notably, the electric field enhancement reaches

much higher values for lower grating pitch, going from a maximum of 3 for a=4 µm to 12 when a=0.4 µm. Moreover, decreasing the grating periodicity amounts to damp the angle-of-incidence dispersion of hyperbolic modes due to the light momentum becoming smaller compared to the grating momentum contribution. Our simulations of CNT gratings of different periodicities by varying the angle of incidence (displayed in Fig. S15) confirm this trend: the calculated reflectance are modified when varying the angle of incidence to a lesser degree with small grating periods are considered.

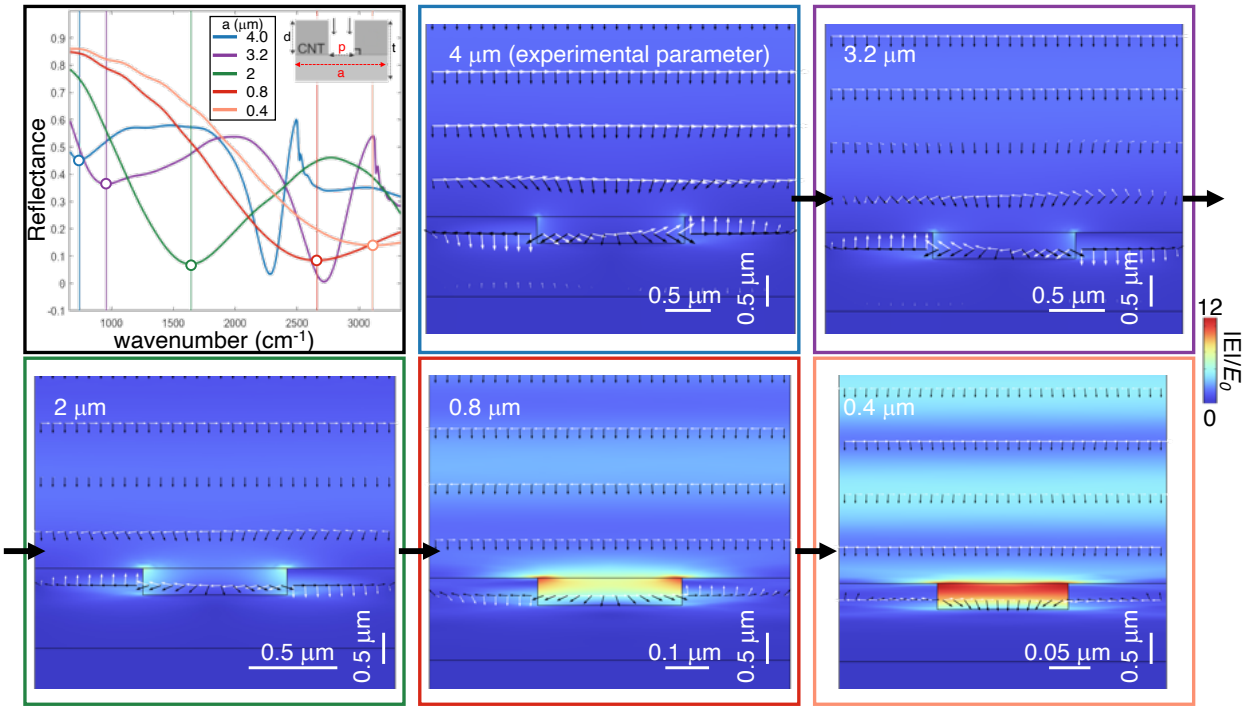

Figure S14: Reducing CNT grating periodicity. Top left: calculated reflectance spectra as a function of the CNT grating periodicity, from the experimental value (pitch a=4 µm, groove width p=1.6 µm) to a=3.2 µm (p=1.28 µm), a=2 µm (p=0.8 µm), a=0.8 µm (p=0.32 µm), a=0.4 µm (p=0.16 µm). Empty dots highlight the dip associated with the confined hyperbolic mode in each curve. From middle top to bottom right: the electric field enhancement spatial distribution evaluated at the corresponding confined HPM frequency (empty dots in the spectra) is shown for each structure after the corresponding geometrical change. White arrows display the electric vector field, black arrows represent the Poynting vector.

To determine the dispersion relation of these confined hyperbolic modes, we followed the approach reported in previous works dealing with similar systems.[7,8] Although the exact same theoretical treatment cannot be applied (in ref.,[7,8] the antennas on a dielectric sub-

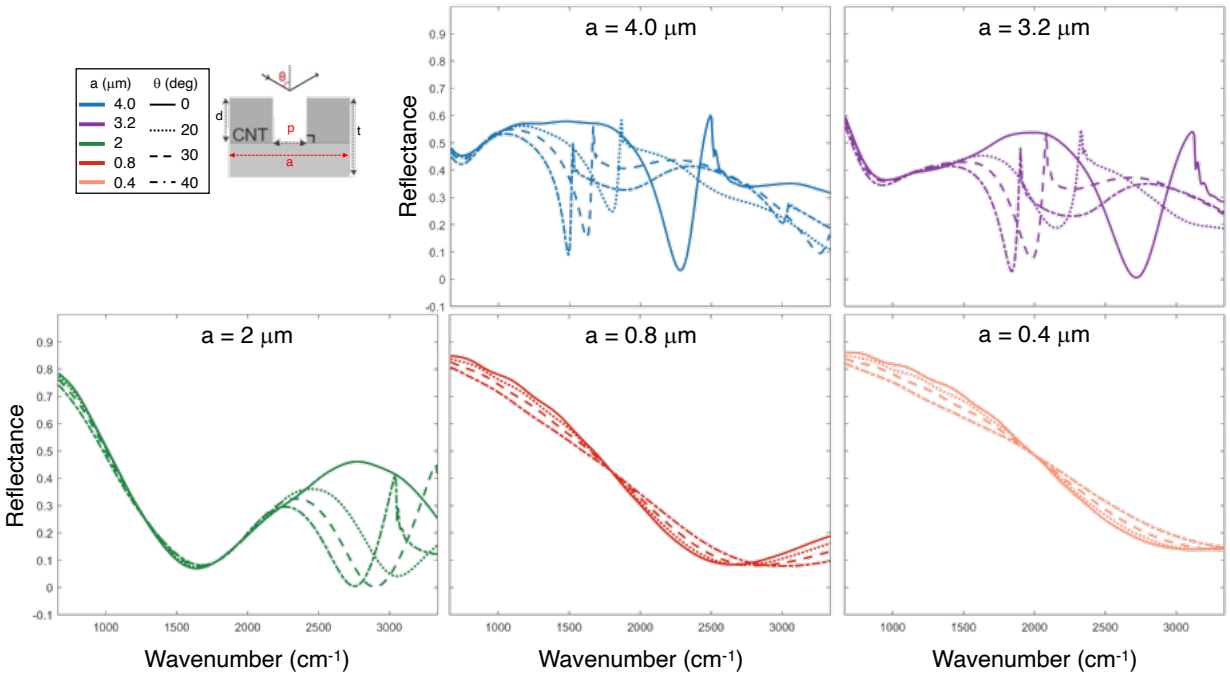

Figure S15: Simulated reflectance of the CNT grating with varying periodicity (a = 4, 3.2, 2, 0.8, 0.4 µm in blue, purple, green, red, and orange, respectively) for different angles of incidences ($\theta = 0°$, 20°, 30°, 40° in solid, dotted, dashed, dash-dotted lines respectively).

strate confining the modes could be rigorously described in the framework of guided mode resonances, while the fact that our hyperbolic grating is made of the same hyperbolic material as the rest of the film hinders a straightforward analytical calculation of the allowed, guided modes in the system), the mechanism of FP-antenna resonances confining hyperbolic modes which would otherwise propagate across the anisotropic bulk is expected to be comparable in the two systems.

Therefore, we performed simulations to track the resonant frequency of the mode under consideration, i.e. the lowest-order FP-confined HPM, upon variations of the groove length (in the x direction, $L = a - p$, where a is the grating period and p the air width). This quantity acts as the relevant length for the Fabry-Pérot resonance to establish across the antenna. The spectra computed in our simulations are reported in Fig. S16 for a grating of periodicity $a = 4\,\mu\text{m}$ and varying p (hence varying $L = a - p$), in the lossless case ($\alpha = \varepsilon''^{\text{FEM}}_{zz}/\varepsilon''^{\text{exp}}_{zz} = 0$), The case of non-zero losses, $\alpha = 1$, gave equivalent results in terms

of spectral position of the analysed peaks).

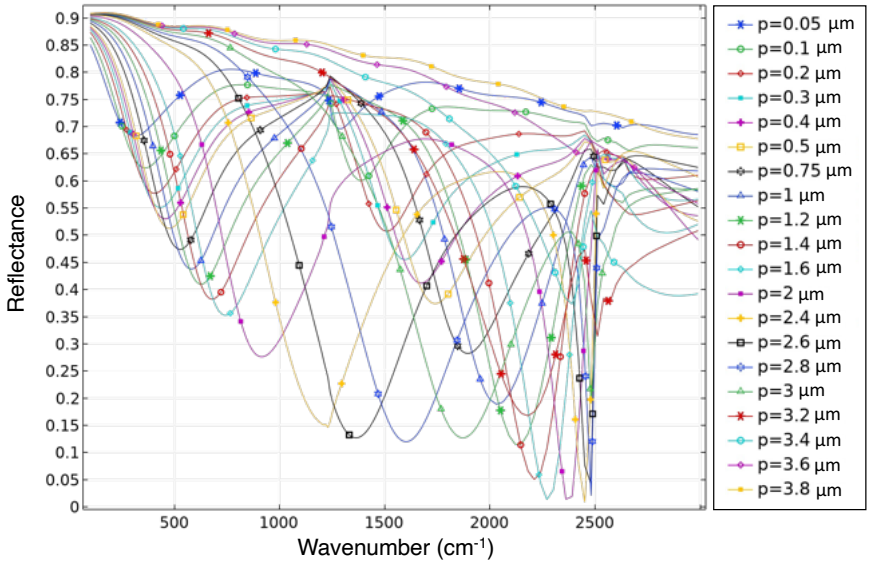

Figure S16: Simulated spectra for the etched CNT film with grating period $a = 4\,\mu\text{m}$ and varying p, assuming zero losses and thickness $d = 0.4\,\mu\text{m}$

Then, starting from the numerical spectra of the CNT film for varying groove width L, the mode wave-vector was then estimated as in,[7] namely $\beta = (\pi - \phi)/L$, where ϕ represents the reflection dephasing and its value has been approximated utilizing the data from ref.[7] It should be noted that the value of ϕ does not change the trend but only shifts the curve laterally. The results of our estimations are reported in Fig. S17 for the case of grating with $4\,\mu\text{m}$ periodicity and varying p (thereby varying L), where the light line ($k_0 = \omega/c$) and the dispersion relation for the fundamental bulk plasmon polariton (BPP, see also Section S7) are reported for comparison.

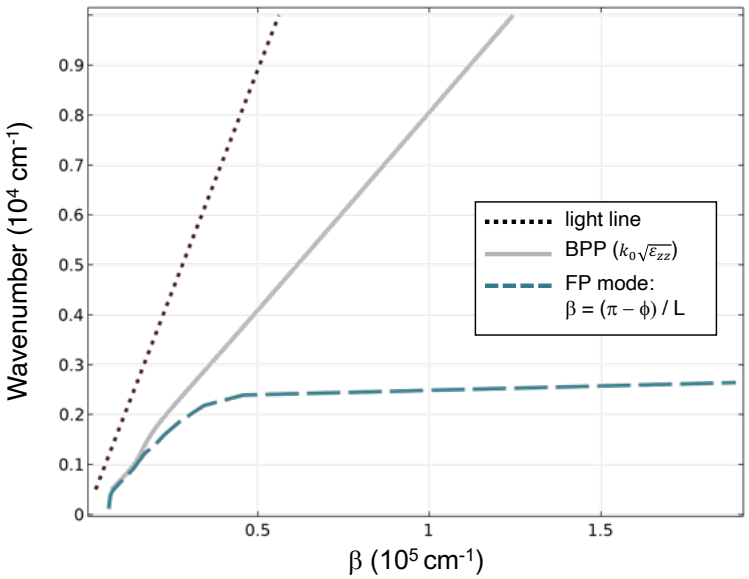

Figure S17: Estimated dispersion relation for the polaritonic FP antenna resonances, confining HPMs in the system, according to ref.[7] The light line (black) and analytical bulk plasmon polariton dispersion (gray) are also shown for comparison.

The so-obtained dispersion for the lowest-order FP confined mode follows relatively well the analytical BPP dispersion relation, at least at low frequencies, far enough from any other electromagnetic resonant feature (surface plasmon polariton, Rayleigh anomaly) we observed across the simulated spectra. For the same reason of different modes overlapping across the spectrum, it was not possible to track the dispersion of higher-order hyperbolic FP resonances. Note however that the estimated mode wave-vector β lies (similarly to the BPP) well below the light line. This indicates the mode analysed is highly confined.

Finally, we highlight that the characteristic response of the system is an inherent feature of the anisotropic optical properties of our sample. To substantiate this aspect,additional simulations were performed to compare the optical response of our CNT film (in the case of a grating periodicity of 3 µm, 30° angle of incidence, grating thickness 0.4 µm) with an equivalent structure having isotropic (purely metallic, $\varepsilon_{xx} = \varepsilon_{zz}$) properties. The obtained reflectance spectra (shown below, Fig. S18) demonstrate that the dip observed in the CNT, that we ascribed to a confined HPM excitation, disappears when an isotropic medium is considered.

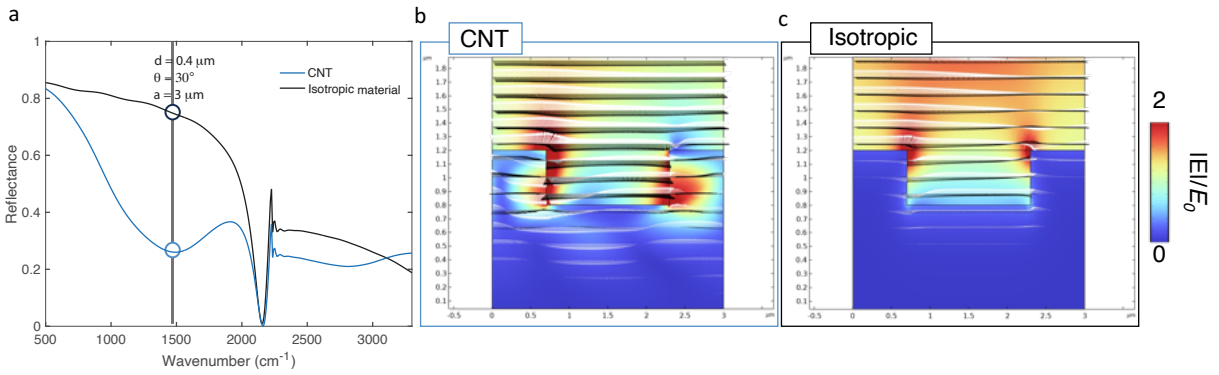

Figure S18: a) Reflectance spectra for the anisotropic CNT film (grating periodicity 3 µm, grating thickness 0.4 µm, angle of incidence 30°, blue line) and the same structure with isotropic optical properties ($\varepsilon_{xx} = \varepsilon_{zz} = \varepsilon_{yy} < 0$). The dip in reflectance observed for the anisotropic case disappears for the isotropic case. b,c) The field enhancement spatial patterns across the structure with either anisotropic (b) or isotropic (c) properties reveal the mode (highlighted by empty circle in the spectra) is highly confined within the grating antennas only when anisotropic permittivity tensor is considered. White arrows represent the electric field, black arrows the Poynting vector.

By looking more in detail to the field pattern of the mode, we could confirm it is highly localised within the CNT grating antennas, as shown by the field enhancement spatial maps. Quantitatively, the spatial integral of the field enhancement over the grating domain is 6 times higher for the anisotropic case compared to the isotropic counterpart. This numerical result points to the spatial confinement of the observed mode within the CNT domain.

S7: Plasmon polaritons (PPs) in the CNT film and their dispersion: bulk and surface PPs.

Thanks to the hyperbolic character of the etched CNT film under investigation, our system can in principle support also bulk plasmon polaritons (BPPs). These modes propagate in the x direction with zero out-of-plane (k_z) momentum component, and they generally require an additional contribution (provided by the grating, in our configuration) to the in-plane (k_x) momentum component to be launched with a well-defined dispersion relation, which streams

from the one holding in the film volume (Eq. 1 from the main text, when $k_z = 0$) and reads (for the fundamental mode) as[9] : $k_x = k_0\sqrt{\varepsilon_{zz}}$, with k_0 the incident light wave-number and ε_{zz} the zz component of the CNT permittivity tensor.

However, BPPs are strongly affected by the material losses, which severely hinders their excitation upon illumination. For this reason, they are not contributing to any sizeable extent to the measured spectra of the sample. Even in simulations, when losses are fictitiously turned off (the imaginary component of the permittivity tensor component ε_{zz} is manually set to zero), these BPPs are predicted to carry a relatively small amount of power. To promote their excitation and enhance their contribution across the calculated spectra, we performed additional numerical simulations for a finite geometry, i.e. without modeling a perfectly periodic infinite array of CNT grooves.

In particular, we considered 10 grooves (as simulations showed that their behaviour is essentially equivalent to that of an infinite array) and performed scattering simulations to explicitly compute the power carried away from the CNT film right below the grooves, which is expected to be associated with BPP excitation. To do so, we integrated the Poynting vector at the sides of the finite grating. The so-obtained spectra for the exemplary cases of groove thickness d=0.4 µm periodicity a=4 µm and a=5 µm, air width between grooves p=1.6 µm and $\theta = 0°$ (see schematic in Fig. S19a) are shown in Fig. S19b.

The strongest contribution observed across the spectrum of the integrated power (carried by the Poynting vector) remains the surface plasmon polariton (SPP). Note that, also in these simulations, its spectral position matches the analytical dispersion we computed according to Eq. S10. Besides the SPP dip, additional, weaker but non-zero modes arise. We interpret these additional features as BPPs, since the observed peaks appear at spectral positions which precisely match the anticipated analytical dispersion of these modes, as illustrated in Fig. S19c.

Moreover, we repeated the same calculations for an angle of incidence of 30° and a grating period of 4 µm. The results of the simulations are reported in Fig. S20. In these conditions,

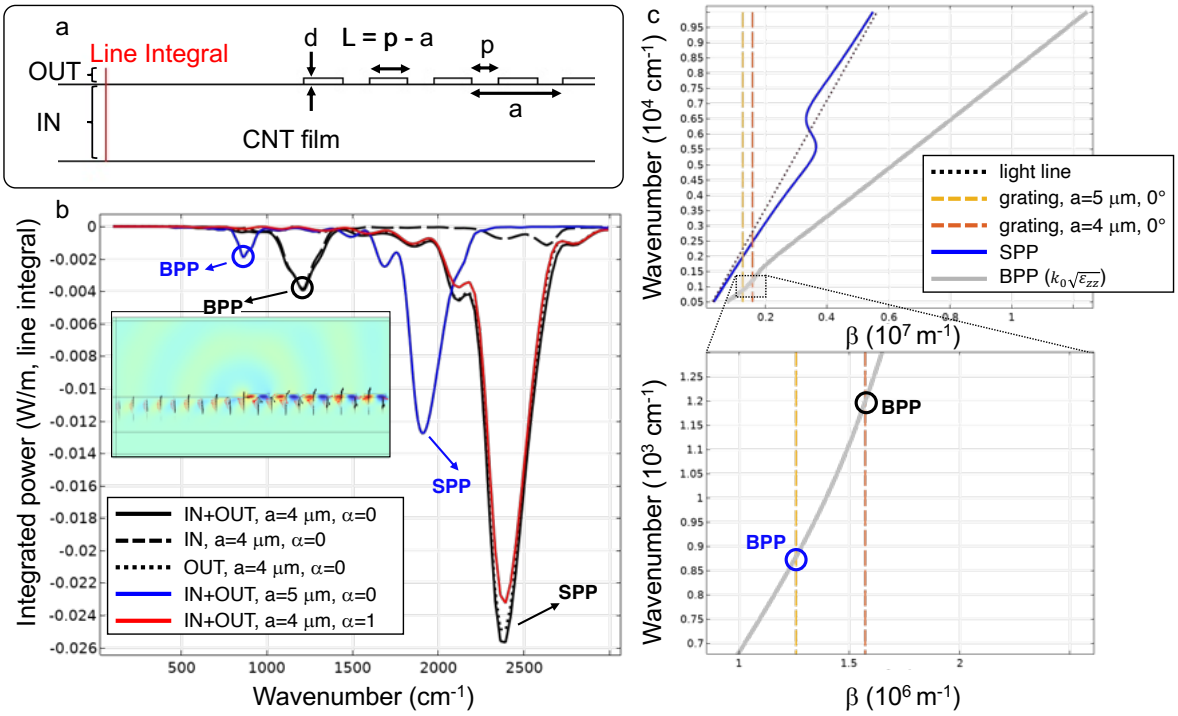

Figure S19: a). Schematic of the system considered in the simulations, with relevant geometrical quantities and a sketch of the line integral used to compute the power carried away from the CNT film. b). Spectra of the integrated [over the line integral highlighted in (a)] Poynting vector for different configurations. SPP and BPP peaks are marked. For the BPP excited by a 4 µm-grating, the electric field spatial pattern is also shown (black arrows indicate the electric vector field, red arrow the Poynting vector). Negative power values are due to the x-axis orientation pointing to the right, opposite to these SPP and BPP excitations. c) Dispersion relations of SPP and BPP, together with light line and grating momentum contributions. The analytical relations match well with the peaks observed in the full-wave simulations.

modes associated with both the +1 and −1 contributions arising from the grating can be excited in the case of BPPs, the degeneracy of which is lifted. This is not the case of SPP, for which the -1 mode is the only one falling in the spectral range under consideration, while the +1 counterpart is at higher frequencies, beyond the simulated spectrum.

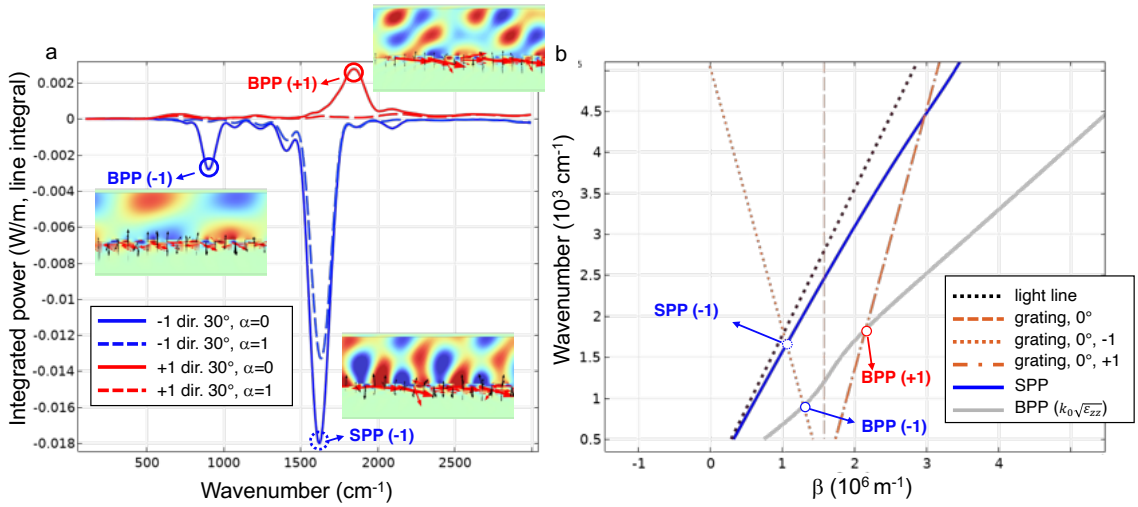

Figure S20: a) Spectra of the integrated Poynting vector for an angle of incidence of 30°, $a = 4\,\mu\text{m}$. SPP and BPP peaks are marked, alongside the (± 1) direction of the grating momentum contribution. For these modes, the electric field spatial pattern is also shown (black arrows indicate the electric vector field, red arrow the Poynting vector). b) Dispersion relations of SPP and BPP, together with tilted (± 1) light line and grating momentum contributions. The analytical relations match well with the peaks observed in the full-wave simulations.

References

(1) Ferrari, L.; Wu, C.; Lepage, D.; Zhang, X.; Liu, Z. Hyperbolic metamaterials and their applications. *Progress in Quantum Electronics* **2015**, *40*, 1–40.

(2) Yan, R.; Wang, T.; Wang, H.; Yue, X.; Wang, L.; Wang, Y.; Zhang, J. Effective excitation of bulk plasmon-polaritons in hyperbolic metamaterials for high-sensitivity refractive index sensing. *Journal of Materials Chemistry C* **2022**, *10*, 5200–5209.

(3) Hutley, M. C. *Diffraction gratings*; Academic Press, 1990.

(4) Cortes, C.; Newman, W.; Molesky, S.; Jacob, Z. Quantum nanophotonics using hyperbolic metamaterials. *Journal of Optics* **2012**, *14*, 063001.

(5) Guo, P.; Diroll, B. T.; Huang, W.; Zeng, L.; Wang, B.; Bedzyk, M. J.; Facchetti, A.; Marks, T. J.; Chang, R. P.; Schaller, R. D. Low-loss near-infrared hyperbolic metamaterials with epitaxial ITO-In2O3 multilayers. *Acs Photonics* **2018**, *5*, 2000–2007.

(6) Maier, S. *Plasmonics - Fundamentals and Applications*; Springer, 2007.

(7) Roberts, J. A.; Yu, S.-J.; Ho, P.-H.; Schoeche, S.; Falk, A. L.; Fan, J. A. Tunable hyperbolic metamaterials based on self-assembled carbon nanotubes. *Nano Letters* **2019**, *19*, 3131–3137.

(8) Roberts, J. A.; Ho, P.-H.; Yu, S.-J.; Wu, X.; Luo, Y.; Wilson, W. L.; Falk, A. L.; Fan, J. A. Multiple tunable hyperbolic resonances in broadband infrared carbon-nanotube metamaterials. *Physical Review Applied* **2020**, *14*, 044006.

(9) Sreekanth, K. V.; Luca, A. D.; Strangi, G. Experimental demonstration of surface and bulk plasmon polaritons in hypergratings. *Scientific reports* **2013**, *3*, 1–7.